Nano Research

ISSN 1998-0124 CN 11-5974/O4
https://doi.org/10.26599/NR.2026.94908737

Research Article

Construction of $Fe^{\delta+}$–$Ru^{\delta-}$ synergistic interface enabling efficient and stable hydrogen evolution in versatile electrolytes

Min Yu, Ziqin Xu, Yuyue Wang, Hao Chen, Kuaibing Wang, Hongjing Zhu, Yi Song, Changyun Chen(✉), Guangxiang Liu(✉)
Jiangsu Key Laboratory of Zero-Carbon Energy Development and System Integration, Nanjing Xiaozhuang University, Nanjing 211171, China

Nano Res., **Just Accepted Manuscript** • https://doi.org/10.26599/NR.2026.94908737
https://www.sciopen.com/journal/1998-0124 on Apr. 15, 2026

Just Accepted

Nano Research

Open Access

Research Article

Construction of $Fe^{\delta+}$–$Ru^{\delta-}$ synergistic interface enabling efficient and stable hydrogen evolution in versatile electrolytes

Min Yu, Ziqin Xu, Yuyue Wang, Hao Chen, Kuaibing Wang, Hongjing Zhu, Yi Song, Changyun Chen ✉, and Guangxiang Liu ✉

Jiangsu Key Laboratory of Zero-Carbon Energy Development and System Integration, Nanjing Xiaozhuang University, Nanjing 211171, China

Received: 12 February 2026; **Revised:** 9 April 2026; **Accepted:** 15 April 2026

✉ Address correspondence to Changyun Chen, cychen@njxzc.edu.cn; Guangxiang Liu, liugx@njxzc.edu.cn

Cite this article: *Nano Research*, 2026, 19, 94908737 https://doi.org/10.26599/NR.2026.94908737

ABSTRACT: Electrocatalytic water splitting for hydrogen production is an important pathway for achieving sustainable green hydrogen production. However, the shortage of freshwater resources limits its large-scale application, making it urgent to develop efficient and stable catalysts suitable for complex water sources such as seawater and wastewater. In this study, a FeRu bimetallic nanocatalyst (FeRu-ERBC) was constructed through biomass-derived two-dimensional porous carbon supports. It demonstrated excellent hydrogen evolution performance in alkaline, seawater, and chemical wastewater environments: with an overpotential of only 22.7 mV (10 mA cm^{-2}) in 1.0 M KOH and over 120 hours of operational stability. Structural characterization and mechanistic studies, complemented by density functional theory (DFT) calculations, revealed that the support not only provides a high specific surface area and mass transport channels but also promotes atomic-level replacement of Fe by Ru, forming a tightly coupled Fe-Ru interface. X-ray photoelectron spectroscopy and in situ spectroscopy confirmed the electronic transfer from Fe to Ru at the interface, forming a "$Fe^{\delta+}$–$Ru^{\delta-}$" synergistic active center. This structure induced the regulation of the surface interfacial water network, thereby enhancing the overall reaction kinetics. This work provides a new strategy for the design of Ru-based catalysts with interface electronic regulation for real-world water environments and highlights the crucial role of biomass carbon supports in advancing green hydrogen technology.

KEYWORDS: hydrogen evolution reaction, biomass-derived carbon, FeRu bimetallic, interfacial electronic engineering

1 Introduction

The continuous growth of global energy demand and the urgent need to address climate change have made hydrogen a key clean energy carrier for achieving a sustainable future. The production of green hydrogen through electrochemical water splitting driven by renewable energy offers a promising pathway [1-3]. However, the issue of the large amounts of freshwater required for large-scale electrolysis has become a major sustainability challenge due to the scarcity of clean water resources worldwide [4,5]. Utilizing abundant alternative water sources, such as seawater or industrial wastewater, provides a viable solution [6-8]. However, this shift presents severe challenges for electrocatalysts, as impurities in complex electrolytes (such as chloride ions, organic compounds, and metal ions) can poison active sites, accelerate corrosion, and lead to structural degradation [9,10]. Therefore, developing hydrogen evolution reaction (HER) electrocatalysts with high activity and excellent durability is crucial for advancing a practical hydrogen economy [11-14].

Ru has become the most ideal substitute for platinum due to its superior hydrogen binding energy and lower cost [15,16]. Particularly in alkaline media compatible with mature anion exchange membrane technology, Ru exhibits a lower hydrolysis potential, which aids the initial Volmer step [17]. However, Ru-based catalysts often face a trade-off between activity and stability, failing to meet the demands of practical applications [18]. The strong interaction of Ru with hydrogen often results in slow hydrogen desorption kinetics. Additionally, in alkaline conditions, the strong chemical adsorption of hydroxyl species permanently poisons active sites [19]. Furthermore, Ru itself has a strong Ru-O covalent bond and lattice oxygen participation, leading to excessive oxidation and irreversible structural collapse during operation [20]. Despite efforts to adjust the electronic structure of Ru through strategies such as heteroatom doping, strain engineering, and constructing strong metal-support interactions (SMSI), numerous challenges remain [21-25]. These factors include complex synthesis processes, insufficient interface coupling, and nanoparticle aggregation/separation phenomena, especially in corrosive environments [26,27]. Therefore, constructing a synergistic electronic environment is crucial.

The choice of support material plays a decisive role in determining the dispersion of metals, interface structure, and the final catalytic performance [28]. Traditional carbon supports, such as carbon black, typically come from the petrochemical industry and often have limited tunability. In contrast, biomass-derived carbon materials provide a

sustainable and structurally adjustable platform [29]. Their inherent heteroatom doping and complex texture can be used to design ordered SMSI. Their natural hierarchical structure and self-templating properties enable the synthesis of high surface area, defect-rich, and inherently N-doped two-dimensional porous carbon matrices (ERBC) [30-32]. This customized structure is considered an ideal substrate for stabilizing ultra-small bimetallic nanoparticles and contributes to effective interface electronic regulation.

In this work, we designed and synthesized a hybrid catalyst anchored by Fe–Ru composite nanoparticles onto engineered biomass-derived carbon (FeRu-ERBC). The ERBC support not only ensures the high dispersion of the metals, but also facilitates the near-complete substitution of Fe by Ru, forming a tight Fe–Ru interface. The electron redistribution from Fe to Ru generates $Fe^{\delta+}$ (electron-deficient) and $Ru^{\delta-}$ (electron-rich) sites. The "$Fe^{\delta+}$–$Ru^{\delta-}$" synergistic effect effectively regulates the hydrogen bond network at the interface, influencing the distribution of water at the interface and thus accelerating reaction kinetics. We systematically evaluated the hydrogen evolution reaction performance of FeRu-ERBC in alkaline media, alkaline seawater, and alkaline chemical wastewater, demonstrating its outstanding activity and durability. Through spectroscopic analysis and in situ testing, we elucidated the critical role of biomass carbon in driving the formation of the synergistic interface and regulating interfacial water behavior. This study provides a reliable approach for designing adaptive electrocatalysts suitable for practical hydrogen production and highlights the application potential of biomass-derived carbon in advanced energy conversion technologies.

2 Experimental

2.1 Pretreatment

Spread the Equisetum ramosissimum Desf evenly on aluminum foil, rinse thoroughly with distilled water, and dry in an oven at 60°C to remove moisture. Place the dried Equisetum ramosissimum Desf in a ceramic boat and calcine it in a tube furnace (under argon atmosphere, heating rate: 5°C/min, target temperature: 300°C, hold for 1 h). After calcination, take out the material and grind it into powder to obtain the pretreated Equisetum ramosissimum Desf material.

2.2 Preparation of Fe-ERBC precursor

Take 0.3000 g of pretreated Equisetum ramosissimum Desf material, 0.3000 g of zinc chloride powder, and 0.9000 g of $FeCl_3$, place them in a ceramic boat, and grind until a paste-like consistency is achieved. Transfer the ceramic boat into a tube furnace and calcine (under N_2 atmosphere, heating rate: 5 °C/min, target temperature: 800 °C, hold for 2 h). After calcination, remove the product, grind it into powder, and add 10% nitric acid while stirring for 2 minutes. Then, wash the material by suction filtration with distilled water until neutral pH is reached. Dry the washed material in a vacuum oven for 2 days to obtain the Equisetum ramosissimum Desf precursor material.

2.3 Preparation of FeRu-ERBC

Take 0.0250 g of Equisetum ramosissimum Desf precursor material and 0.0150 g of $RuCl_3$, place them in a ceramic boat, and mix thoroughly by grinding. Transfer the mixture into a tube furnace and calcine (under Ar atmosphere, heating rate: 2 °C/min, target temperature: 450 °C, hold for 1 h). After cooling, collect the final product to obtain the Ru-modified Equisetum ramosissimum Desf sample.

3 Results and discussion

The synthetic schematic shown in Figure 1a illustrates the carrier-guided precise interface construction strategy. In contrast to traditional co-impregnation methods, this work employs a step-by-step synthesis approach: first, an Fe-ERBC precursor with highly dispersed Fe species is constructed (Figures S1 and S2), followed by the formation of the Fe–Ru interface at predefined positions through a substitution reaction with Ru^{3+}. In order to clarify the unique role of biomass-derived carbon supports, we simultaneously prepared the control sample FeRu-AC using commercial activated carbon (AC) as the support. The Transmission electron microscopy (TEM) image of FeRu-ERBC in Figure 1b shows that the ultrafine nanoparticles are highly uniformly dispersed on the two-dimensional porous carbon support, with no apparent aggregation. The particle size distribution statistics based on measurements of more than 60 particles indicate an average size of 2.22±0.5 nm (Figure S3). This high dispersion is directly attributed to the strong anchoring effect of the surface defects and functional groups of the biomass carbon support on the metal precursor. The control sample FeRu-AC prepared simultaneously also shows nanoparticle dispersion on commercial AC (Figure S4). The X-ray diffraction (XRD) patterns (Figures 1c and S5) comparison reveals a fundamental transformation in the catalyst's crystal structure [33]. The diffraction peaks associated with Fe species in Fe-ERBC almost completely disappear in FeRu-ERBC, leaving only the characteristic peak of (101) crystal plane to metal Ru. To quantitatively analyze this transformation, Rietveld refinement was performed on the XRD data (Figure S6), confirming that the Fe-related phases fall below the detection limit (<1 wt%), while the metallic hcp Ru (P63/mmc) constitutes the predominant crystalline component. Combined with the decrease in Fe content measured by ICP-OES (Table S1), it is confirmed that on the biomass carbon support, the initial Fe species have been almost entirely atomically substituted and integrated by Ru, rather than forming a physically mixed heterogeneous structure. The FeRu-AC retains a prominent Fe_3O_4 diffraction peak (Figure S7) [34], and ICP-OES shows that its Fe residue is significantly higher proving that the substitution reaction on commercial activated carbon is incomplete, and a similar Ru phase structure has not been formed. The atomic-level structure was further clarified through high-angle annular dark-field scanning TEM (HAADF-STEM). The fast Fourier transform (FFT) spectrum obtained from the region marked in Figure 1d confirmed the good crystallinity of the supported nanoparticles, consistent with the hexagonal Ru phase identified by XRD [35]. Additionally, high-resolution TEM (HRTEM) images (Figures 1e and S8) clearly display lattice fringes with a measured spacing corresponding to the (101) plane of metallic Ru [36]. The energy-dispersive X-ray

spectroscopy (EDS) elemental mapping in Figure 1f visually confirms the uniform composite and close coexistence of Fe and Ru at the nanoscale in space. The strong overlap of the signals from C, O, Fe and Ru, especially the high consistency in the distribution of Fe and Ru, confirms the successful construction of bimetallic composite nanoparticles.

Further investigation into the surface structure and electronic state of the catalyst was conducted. Figure 2a compares the Raman spectra of Fe-ERBC and FeRu-ERBC. FeRu-ERBC exhibits a higher I_D/I_G ratio (1.00), indicating that the introduction of Ru increases the defect density in the carbon framework, which is a key characteristic of the ERBC support and is beneficial for enhanced charge transfer and catalytic activity [37]. N_2 adsorption-desorption tests were used to analyze the pore structure of the materials. As shown in Figure 2b, both Fe-ERBC and FeRu-ERBC display a mixed isotherm of type I and type IV, with rapid adsorption in the low-pressure region and a distinct H4-type hysteresis loop, confirming the presence of micropores and mesopores. The corresponding pore size distribution curve (Figure 2c) further demonstrates their well-developed porous characteristics. The high specific surface area of FeRu-ERBC (993.47 m^2 g^{-1}) is substantially higher than that of commercial activated carbon (425.43 m^2 g^{-1}, Figure S9), and its developed pore structure together facilitate mass transfer and exposure of active sites during the reaction process. In contrast, the pore structure of FeRu-AC is mainly microporous, with insufficient mesopore development and fewer surface oxygen-containing functional groups. This limits the mass transfer efficiency and the full exposure of active sites during the reaction process [38].

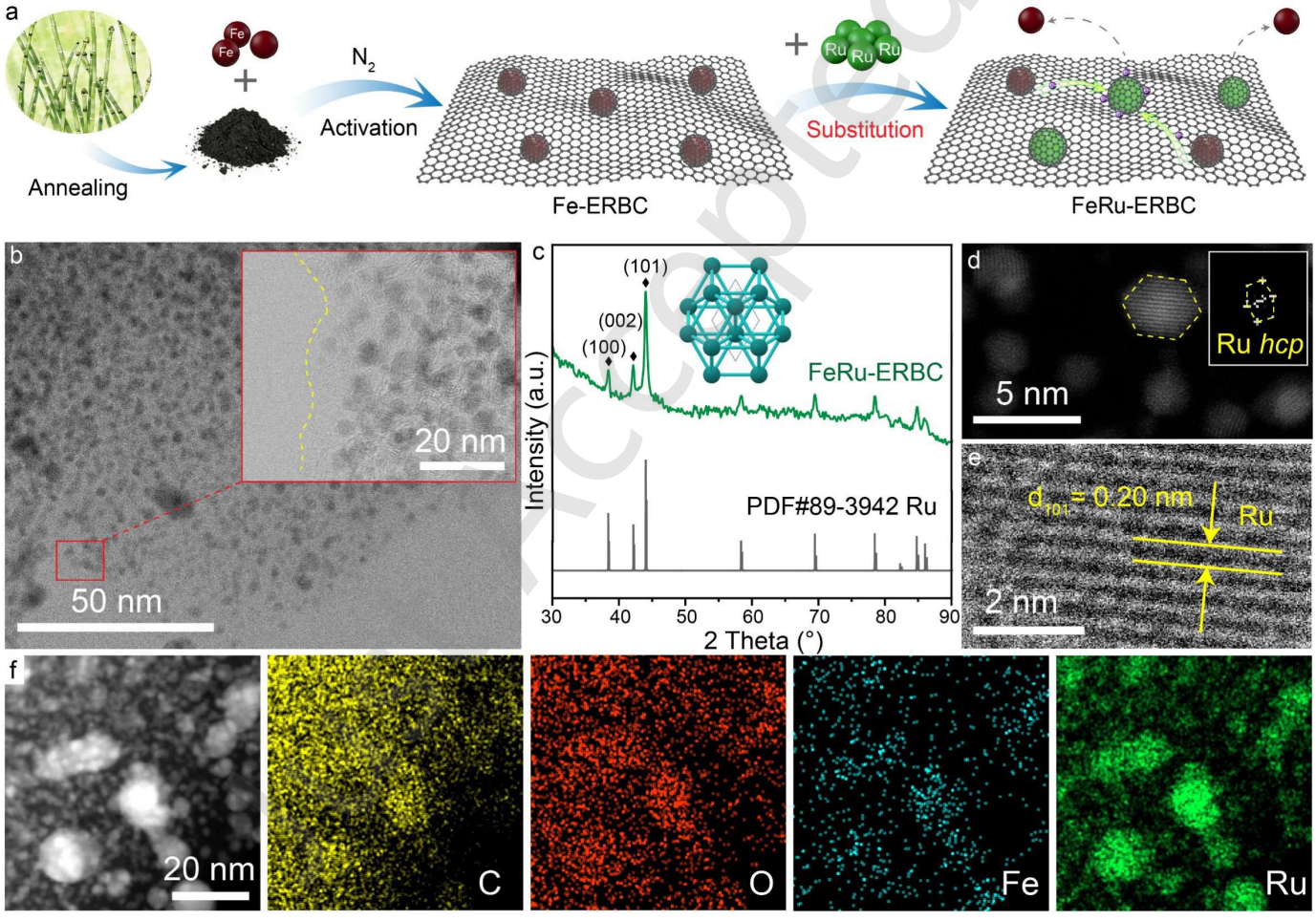

Figure 1 (a) Schematic illustration of the synthesis process of FeRu-ERBC. (b) TEM image of FeRu-ERBC. The inset shows a magnified view of the selected area. (c) XRD patterns of Fe-ERBC and FeRu-ERBC. (d) HADDF-STEM image and (e) HRTEM image of FeRu-ERBC. The inset in (d) displays the corresponding FFT pattern. (f) EDS elemental mapping of FeRu-ERBC.

X-ray photoelectron spectroscopy (XPS) was used to deeply analyze the surface elemental chemical states and electronic transfer (Figure S10). The high-resolution Fe 2p spectrum (Figure 2d) shows that, compared to Fe-ERBC, the Fe 2p binding energy in FeRu-ERBC undergoes a positive shift of about 0.68 eV, indicating a reduction in electron density around Fe [39]. Meanwhile, the Ru 3p spectrum (Figure 2e) can be divided into two components, Ru^0 and Ru^{n+}, indicating the coexistence of Ru in both metallic and oxidized states [40]. To more accurately verify the charge redistribution process, high-resolution Ru 3d spectra were collected and deconvoluted (Figure S11). The Ru $3d_{5/2}$ peak is located at 280.2 eV, which is slightly positively shifted relative to the standard binding energy of metallic Ru^0 (280.0 eV), indicating the presence of a minor oxidized state (Ru^{n+}) on the Ru surface, consistent with the Ru 3p results.

The O 1s spectrum (Figure 2f) shows that in FeRu-ERBC, compared to Fe-ERBC, the peak corresponding to the metal–oxygen bond (M–O, approximately 530.1 eV) shifts positively by about 0.58 eV.

The systematic binding energy shift analysis in Figure 2g quantitatively presents this charge redistribution process. The positive shift in Fe 2p binding energy (ΔB.E. ~ +0.68 eV) and the shift in the O 1s (M–O) peak (ΔB.E. ~ +0.58 eV) corroborate each other, providing evidence for the flow of electrons from the Fe–O region, which drives the formation of the "$Fe^{\delta+}$–$Ru^{\delta-}$" local electronic structure. It is worth noting that a positive shift in the Fe 2p binding energy was also observed in FeRu-AC (Figure S12). However, combining XRD phase analysis suggests that in commercial AC, the introduction of Ru did not effectively promote the occurrence of substitution reactions. On the contrary, it may have facilitated the conversion of elemental Fe to Fe_3O_4 during subsequent processing.

Additionally, the peak area ratio analysis in Figure 2h provides quantitative information about the surface chemical states. The Fe 2p spectrum was fitted to yield a Fe^{2+}/Fe^{3+} peak area ratio of 0.82:1 in FeRu-ERBC, indicating a predominance of Fe^{3+}, consistent with electron transfer from Fe to Ru leading to an increased oxidation state of Fe. The Ru 3p spectrum was deconvoluted into two components, Ru^0 and Ru^{n+}, with an area ratio of approximately 1.2:1, confirming the coexistence of metallic and oxidized Ru species; the latter is attributed to slight surface oxidation or strong metal–support interaction. The O 1s spectrum reveals a positive shift of 0.58 eV for the M–O bond (530.1 eV) in

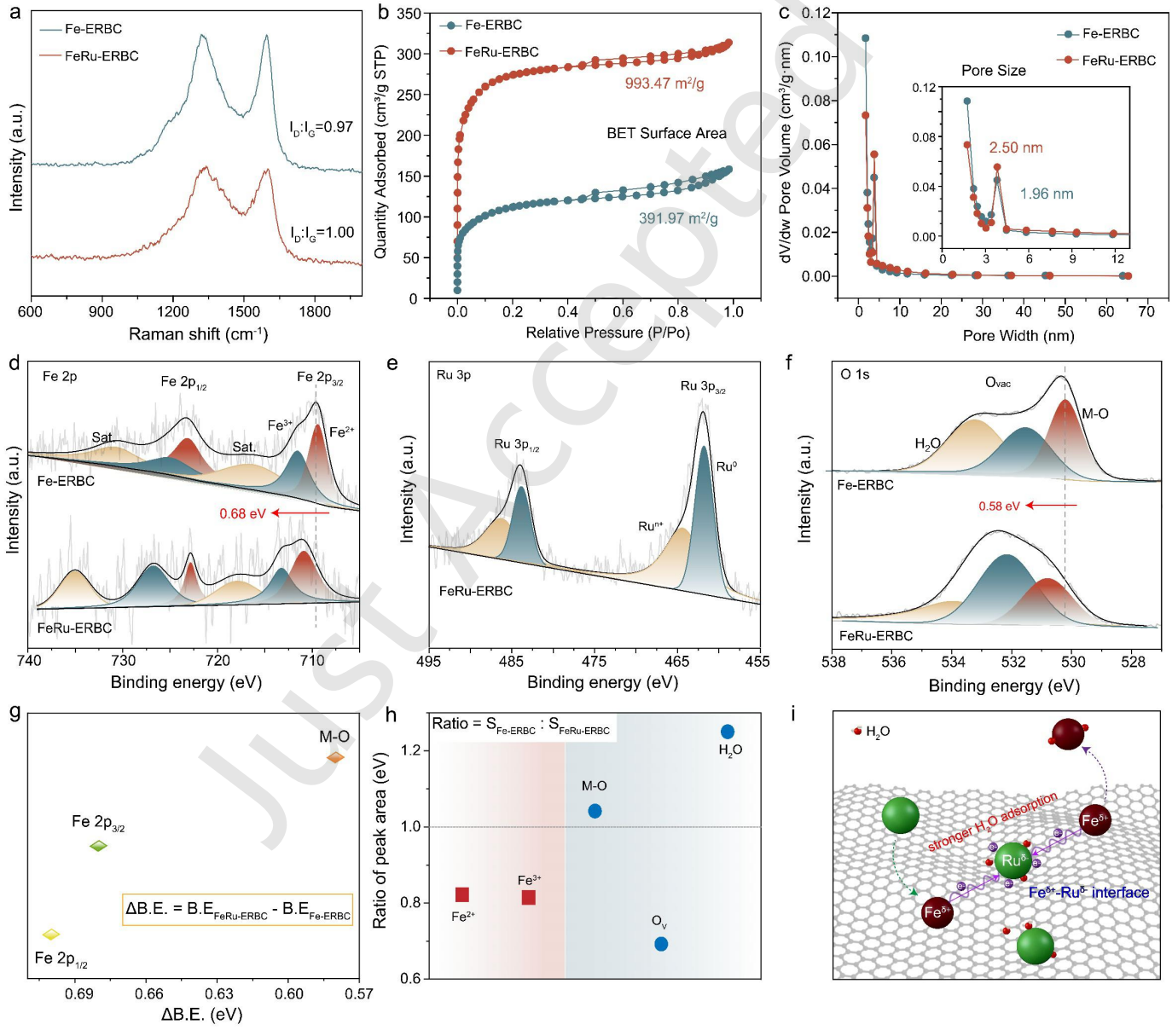

Figure 2 (a) Comparison of Raman spectra for Fe-ERBC and FeRu-ERBC. (b) N_2 adsorption-desorption isotherms of Fe-ERBC and FeRu-ERBC. (c) Corresponding pore size distribution curves of Fe-ERBC and FeRu-ERBC. (d) High-resolution Fe 2p XPS spectra of Fe-ERBC and FeRu-ERBC. (e) High-resolution Ru 3p XPS spectrum of FeRu-ERBC. (f) High-resolution O 1s XPS spectrum of FeRu-ERBC. (g) Binding energy shift analysis derived from the Fe 2p and O 1s XPS spectra. (h) Peak area ratio analysis of different chemical states in FeRu-ERBC. (i) Schematic illustration of the proposed electron transfer process between Fe and Ru based on spectroscopic analysis.

FeRu-ERBC compared to Fe-ERBC, while the peak area ratio remains close to 1, suggesting a reduction in Fe–O bonds accompanied by the formation of new Ru–O bonds, indicative of strong metal–support interaction [41]. Based on the above analysis, Figure 2i provides a clear schematic of electron transfer and synergistic effects. On the biomass carbon support, the more electronegative Ru atoms form atomically level interfaces with Fe atoms via substitution reactions, leading to the transfer of electrons from Fe to Ru. This process results in the formation of $Fe^{\delta+}$ sites with electron deficiency and $Ru^{\delta-}$ sites with electron enrichment, which in turn triggers a series of functionalized interface reconstructions.

The HER performance of FeRu-ERBC was evaluated in N_2-saturated 1.0 M KOH electrolyte. For comparison, FeRu-AC and commercial Pt/C catalysts were also tested under the same conditions. All key electrochemical measurements were repeated at least three times, and standard deviation error bars were added to ensure statistical significance. As shown in Figure 3a and Table S2, FeRu-ERBC requires only a 22.7 mV overpotential to reach a current density of 10 mA cm^{-2}, which is significantly lower than the commercial Pt/C (31.3 mV) and FeRu-AC (65.9 mV). Figures 3b and S13 further summarizes and compares the key HER performance parameters of the two catalysts: FeRu-ERBC exhibits the lowest Tafel slope (29.0 mV dec^{-1}), close to the theoretical value for the Volmer–Heyrovsky mechanism (~30 mV dec^{-1}), indicating optimal HER reaction kinetics. At an overpotential of 50 mV, FeRu-ERBC achieves a mass activity of 224.2 A mg^{-1}, far exceeding that of FeRu-AC (3.4 A mg^{-1}), demonstrating its superior current generation capability per unit mass, which is beneficial for reducing catalyst usage and cost. Additionally, its turnover frequency at the same overpotential reaches 0.75 s^{-1}, significantly surpassing FeRu-AC (0.01 s^{-1}), confirming the higher intrinsic activity of FeRu-ERBC. These results collectively indicate that FeRu-ERBC with a high specific surface area exhibits superior intrinsic catalytic activity in the HER.

As depicted in Figure 3c and Table S3, FeRu-ERBC outperforms various recently reported noble metal-based catalysts in HER activity. In addition to high activity, this catalyst also exhibits remarkable electrochemical stability. After 15,000 cycles of cyclic voltammetry, the overpotential required to reach 10 mA cm^{-2} increases by only 4.3 mV (Figure 3d). Chronopotentiometry tests further demonstrate that FeRu-ERBC shows no noticeable decay after 120 hours of continuous operation at a constant current density of 10 mA cm^{-2} (Figure 3e). TEM image after stability (Figure S14) proved that the strong anchoring effect prevents the aggregation and detachment of Ru nanoparticles during long-term operation. Electrochemical impedance spectroscopy results (Figure 3f) indicate that FeRu-ERBC presents the smallest semicircle diameter in the Nyquist plot at 100 mV overpotential, suggesting the lowest charge transfer resistance. Moreover, double-layer capacitance tests estimate the electrochemical active surface area, indicating that FeRu-ERBC has a larger exposed active site area (Figures 3g and S15), further supporting its superior catalytic performance. To evaluate its industrial applicability, an electrolyzer was assembled using FeRu-ERBC as the cathode catalyst. As shown in Figure S16, its performance was comparable to that of commercial Pt/C, albeit slightly inferior; nevertheless, it maintained stable operation at a current density of 1 A cm^{-2} for over 80 hours.

The growing conflict between the dependence on freshwater resources for large-scale hydrogen production and the scarcity of freshwater resources highlights the potential of directly utilizing seawater or chemical wastewater for hydrogen electrolysis as promising alternatives. To assess the catalyst's applicability in actual complex water sources, this study systematically tested the HER performance of FeRu-ERBC in chemical alkaline seawater and alkaline chemical wastewater environments. As shown in Figure 3h, in seawater prepared with 1.0 M KOH and in 200-fold diluted chemical wastewater, FeRu-ERBC exhibits overpotentials of 35.3 mV and 37.2 mV at a current density of 10 mA cm^{-2}, respectively, demonstrating excellent electrochemical activity. The durability of FeRu-ERBC in complex electrolytes was further tested using cyclic voltammetry and chronopotentiometry (Figures 3i and S17). FeRu-ERBC maintains a stable current density with only a 1.8 mV positive shift in η_{10} after 15,000 sweeping cycles in seawater and a 10.1 mV positive shift after 1,000 sweeping cycles in chemical wastewater. Chronopotentiometry tests indicate that the catalyst exhibits negligible activity decay after 70 hours of continuous operation in alkaline seawater at 10 mA cm^{-2}, while noticeable decay occurs after 10 hours in chemical wastewater. Overall, the stability of the catalyst in wastewater is lower than in seawater, primarily due to the presence of impurities in the chemical wastewater, such as organic compounds and heavy metals, which are adsorbed onto the catalyst surface. This adsorption blocks the active sites, reducing catalytic activity, thereby increasing the electron transfer resistance and lowering the overall efficiency of the electrolysis process.

To further clarify the interfacial dynamic behavior of FeRu-ERBC under electrochemical conditions, electrochemical impedance spectroscopy (EIS) was used to systematically analyze its charge transfer and interfacial processes. Figure S18a shows the Nyquist plot at different applied potentials under 1.0 M KOH. The intercept of the high-frequency region with the real axis corresponds to the solution resistance (R_s), while the single flat semicircle in the mid-frequency region is mainly attributed to the charge transfer process at the electrode-electrolyte interface [42]. As the potential moves from the standard potential in the negative direction, the diameter of the semicircle decreases significantly, indicating that the charge transfer resistance (R_{ct}) decreases with the increase in overpotential, which is characteristic of the activation-controlled step in electrocatalytic reactions [43].

Using the Bode plot (Figure S18b) for further analysis, the dynamic information in the frequency domain can be more clearly explained. In the higher frequency range (> ~10^3 Hz), the phase angle approaches zero degrees, and the impedance magnitude is mainly controlled by R_s; in the mid-frequency region (around 10^3 ~ 10^0 Hz), a distinct peak appears in the phase angle, corresponding to the dominance of the charge transfer process within this frequency range. The peak width and height reflect the uniformity of the interface process and

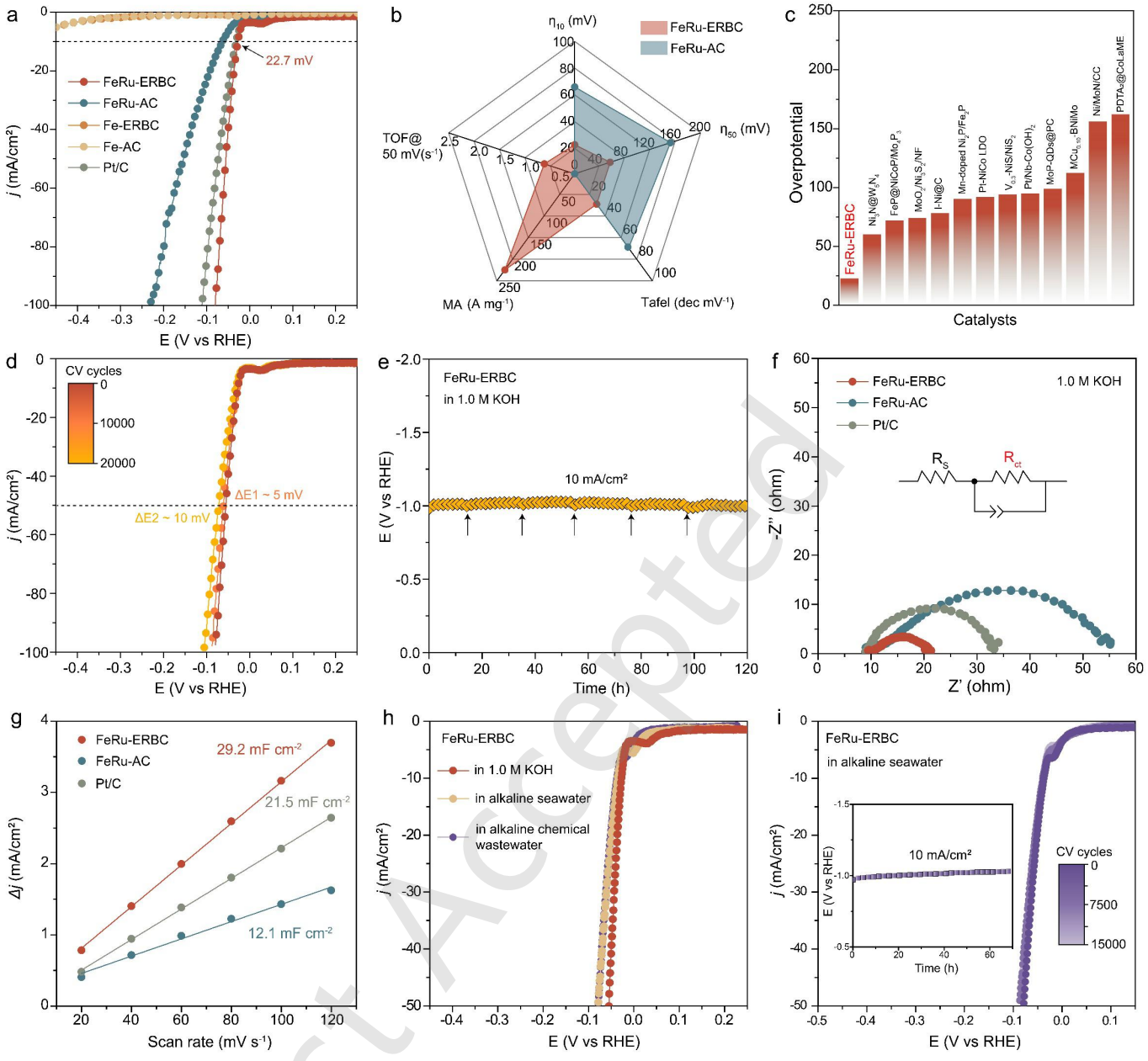

Figure 3 (a) Comparison of HER polarization curves for FeRu-ERBC, Pt/C, and control samples in alkaline medium. (b) Comparison of key HER performance parameters between FeRu-ERBC and Fe-ERBC. (c) Comparison of the overpotential at 10 mA cm^{-2} between FeRu-ERBC and recently reported noble-metal-based HER catalysts. (d) HER polarization curves of FeRu-ERBC before and after multiple cyclic voltammetry scans in alkaline medium. (e) Chronopotentiometry stability test of FeRu-ERBC at 10 mA cm^{-2}. (f) Electrochemical impedance spectroscopy (Nyquist plots) of FeRu-ERBC and control samples at a fixed overpotential. (g) Comparison of double-layer capacitance (Cdl) derived from CV scans at different rates in the non-faradaic region. (h) Comparison of HER polarization curves for FeRu-ERBC measured in alkaline pure water, alkaline seawater, and alkaline chemical wastewater. (i) Cyclic voltammetry cycling stability test of FeRu-ERBC in alkaline seawater; the inset shows the corresponding chronopotentiometry test curve.

the distribution of time constants; in the low-frequency region (<10^0 Hz), the phase angle decreases to zero degrees again, and the impedance behavior is gradually influenced by mass transfer or surface intermediate adsorption-desorption processes. In the HER working potential range, FeRu-ERBC exhibits a relatively broad mid-frequency phase angle peak, extending towards the high-frequency direction, indicating that the interfacial charge transfer dynamics are fast, with a smaller distribution of time constants, which also confirmed by the smaller R_{ct} displayed in the Nyquist plot [44, 45].

To investigate the effect of electrolyte complexity on interfacial dynamics, comparative EIS experiments were conducted in seawater and chemical wastewater (Figures S19-S21). The R_{ct} and total polarization resistance (R_p) extracted via equivalent circuit fitting (Figures 4a and 4b) indicate that FeRu-ERBC exhibited the lowest and most stable resistance values in all media. Notably, in alkaline seawater and wastewater, there was no significant increase in R_{ct}, suggesting that the interface maintained efficient and stable charge transfer even in the presence of Cl^- and organic soil impurities. This outstanding impedance performance

can be attributed to its "$Fe^{\delta+}$–$Ru^{\delta-}$" synergistic interface, which facilitating rapid charge transfer and preventing interfacial passivation and resistance buildup, thereby sustaining efficient kinetics over a wide frequency range [46, 47].

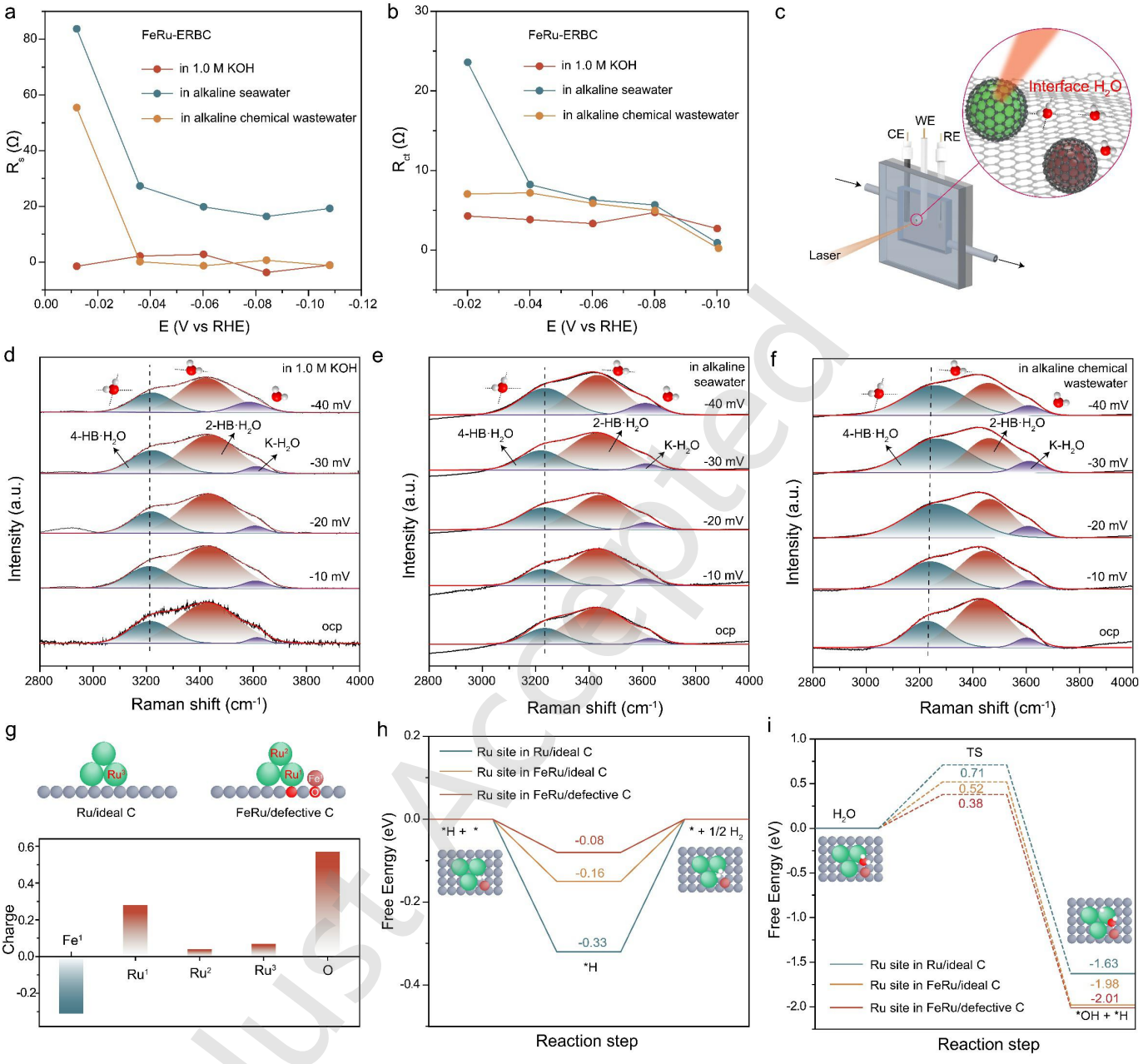

Figure 4 (a) Comparison of the fitted RS values. (b) Comparison of the fitted Rct values. (c) Schematic of the experimental setup for operando Raman spectroscopy measurements. Operando Raman spectra collected during the HER process for FeRu-ERBC in (d) 1.0 M KOH, (e) alkaline seawater and (f) alkaline wastewater. (g) Bader charge analysis of the $Fe^{\delta+}$–$Ru^{\delta-}$ interface. (h) Calculated ΔG_H on different sites. (i) Calculated water dissociation barrier (Volmer step) on different models.

Based on the efficient and stable interfacial charge transfer characteristics revealed by the previous impedance analysis, the molecular structural origins of the interfacial microenvironment were further investigated through operando Raman spectroscopy (Figure 4c), with a focus on the structural evolution of the interfacial water network. Figures 4d-f show the Raman spectra of the O-H stretching vibration region (~3000-3800 cm^{-1}) and their deconvolution fitting results during HER of FeRu-ERBC in different electrolytes. In 1.0 M KOH, as the potential shifts negatively, the intensity of the broad peak corresponding to strongly hydrogen-bonded network water gradually decreases, while the peak representing weak hydrogen bonds or "quasi-free" OH groups relatively increase. To quantify the modulation of the water network, peak deconvolution of the O–H stretching region was performed to differentiate strongly hydrogen-bonded water (~3200 cm^{-1}) from weakly hydrogen-bonded/free OH groups (~3500 cm^{-1}). The peak area ratio A_{weak}/A_{strong} was calculated as a function of applied potential. For FeRu-ERBC in 1.0 M KOH, this ratio increases linearly with negative potential, yielding a slope of 0.015 (Figure S22). This quantitative result demonstrates that the

$Fe^{\delta+}$–$Ru^{\delta-}$ interface effectively loosens the hydrogen-bond network of interfacial water, creating a more dynamic water environment conducive to proton transfer. This "loosened" H_2O network structure is in excellent agreement with the low R_{ct} observed in impedance analysis, as it reduces the energy barrier for H_3O^+ or H_2O transport and activation at the interface.

To provide theoretical validation for the proposed synergistic mechanism, density functional theory (DFT) calculations were performed. The atomic models were constructed based on the experimentally identified structural features, as illustrated in Figure S23. Bader charge analysis on the FeRu/defective C model (Figure 4g) reveals that the Fe atom at the interface loses approximately 0.31 |e|, while the adjacent Ru atom gains about 0.28 |e|, resulting in a net electron transfer of approximately 0.30 |e| from Fe to Ru. This quantitative result is in excellent agreement with the experimentally observed positive shift of the Fe 2p binding energy (+0.68 eV) in XPS, providing direct theoretical evidence for the formation of the $Fe^{\delta+}$–$Ru^{\delta-}$ configuration. The calculated hydrogen adsorption free energy (ΔG_H) values on different models are shown in Figure 4h: on the Ru site in Ru/ideal C (Model 1), ΔG_H = -0.33 eV; on the Ru site in FeRu/ideal C (Model 2), ΔG_H = -0.16 eV; and on the $Ru^{\delta-}$ site in FeRu/defective C (Model 3), ΔG_H = -0.08 eV, which is close to the optimal value (0 eV). These results demonstrate that the $Ru^{\delta-}$ site offers a nearly ideal H adsorption strength. Additionally, the calculated water dissociation barriers (Volmer step: $H_2O \rightarrow H^* + OH^-$) show a progressive decrease (0.71 eV on Ru/ideal C, 0.52 eV on FeRu/ideal C, and 0.38 eV on FeRu/defective C) in Figure 4i, confirming the synergistic mechanism in which $Fe^{\delta+}$ promotes O–H bond cleavage and $Ru^{\delta-}$ stabilizes the adsorbed H intermediate.

In the complex environment of alkaline seawater and wastewater (Figures 4h, i), this spectral evolution trend remains consistent. Despite the presence of Cl^- and organic impurities in the electrolyte, the FeRu-ERBC interface can still induce similar dynamic restructuring of the water network, without the appearance of new peaks that would indicate specific adsorption of pollutants or interfacial water structure. This explains at the molecular scale why its impedance behavior remains stable in complex media. The "$Fe^{\delta+}$–$Ru^{\delta-}$" synergistic interface not only optimizes the adsorption of reaction intermediates at the metal sites, but also maintains a stable and highly active interfacial water layer through its unique surface electric field, serving as a "high-speed channel" for proton transfer, ensuring that the Volmer step ($H_2O + e^- \rightarrow H^* + OH^-$) remains efficient [48, 49].

4 Conclusions

This work successfully developed an efficient and stable HER electrocatalyst, FeRu-ERBC, by anchoring FeRu bimetallic nanoparticles onto a two-dimensional porous carbon support derived from Equisetum ramosissimum Desf. It achieves a current density of 10 mA cm^{-2} with an overpotential of only 22.7 mV in 1.0 M KOH and excellent long-term stability (>120 hours), outperforming commercial Pt/C, in both alkaline seawater and chemical wastewater. Systematic characterization and mechanistic studies reveal that its outstanding performance originates from a unique "$Fe^{\delta+}$–$Ru^{\delta-}$" synergistic catalytic interface directed by the biomass-derived carbon support. This support not only provides a high specific surface area and hierarchical pores to facilitate mass transport but also more critically drives the near-complete substitution of Fe by Ru, resulting in an atomically intimate Fe-Ru interface. The interfacial electronic structure, comprising electron-deficient $Fe^{\delta+}$ sites and electron-enriched $Ru^{\delta-}$ sites, cooperatively optimizes the adsorption behavior of key reaction intermediates and activates the interfacial water network, thereby sustaining rapid reaction kinetics. This designed interface ultimately endows the Ru-based catalyst with high activity in complex environments.

Electronic Supplementary Material: Supplementary material (please provide the brief detail of the ESM) is available in the online version of this article at https://doi.org/10.26599/NR.2026.94908737.

Data availability

All data needed to support the conclusions in the paper are presented in the manuscript and/or the Electronic Supplementary Material. Additional data related to this paper may be requested from the corresponding author upon request.

Acknowledgements

This work was supported by High-Level Cultivation Project of Nanjing Xiaozhuang College (No. 2022NXY04) and Research Program of Jiangsu Provincial Natural Science Foundation of Higher Education Institutions (No. 25KJA150004).

Declaration of competing interest

All the contributing authors report no conflict of interests in this work.

Author contribution statement

M. Y.: Funding acquisition, supervision, experimental design, writing-review & editing. Z. Q. X.: Experiment implementation, formal analysis. Y. Y. W.: Experiment implementation, formal analysis. H. C.: Experiment implementation, formal analysis. K. B. W.: Data curation, analyzed the data. H. J. Z.: Data curation, formal analysis. Y. S.: Analyzed the data. C. Y. C.: Funding acquisition, analyzed the data. G. X. L. Funding acquisition, verified the data accuracy. All the authors have approved the final manuscript.

Informed consent

Not applicable.

Ethics statement

Not applicable.

Use of AI statement

None.

References

[1]Wang, M.; Yan, C.; Liu, T.; Wang, S.; Liao, Z.; Guo, F.; Wang, Q.; Li, Z.; Wang, G. Enhancing built-in electric field via balancing interfacial atom orbit hybridization at boride@sulfide heterostructure for hydrogen evolution reaction. *Angew. Chem. Int. Ed.* **2025**, *64*, e202425657.

[2]Tao, Y.; Lorenz-Ochoa, K. A.; Pan, L.; Al-Mualem, Z. A.; Baiz, C. R.; Ren, H. Tuning the hydrogen evolution reaction activity and mechanism on

Pt via nano-confinement of interfacial water. *J. Am. Chem. Soc.* **2025**, *147*, 29977-29982.

[3]Wang, C.; Yang, Y.; Zheng, J.; Yuan, Y.; Pang, D.; Liu, J.; Wu, H.; Liu, N.; Yang, H. Y.; Pang, X. Magnetic field-driven spin state transformation in promoting the catalytic activity of doped single-atom for hydrogen evolution reaction. *Adv. Mater.* **2025**, e13213.

[4]Wang, M.; Bodirsky, B. L.; Rijneveld, R.; Beier, F.; Bak, M. P.; Batool, M.; Droppers, B.; Popp, A.; van Vliet, M. T. H.; Strokal, M. A triple increase in global river basins with water scarcity due to future pollution. *Nat. Commun.* **2024**, *15*, 880.

[5]Lin, H.; Song, Y.; Ding, Z.; Sui, Y.; Sui, Z.; Li, F.; Zhu, J.; Wu, W. Multi-stage power-to-water battery synergizes flexible energy storage and efficient atmospheric water harvesting. *Nat. Commun.* **2025**, *16*, 11098.

[6]Bao, D.; Huang, L.; Gao, Y.; Davey, K.; Zheng, Y.; Qiao, S.-Z. Dynamic creation of a local acid-like environment for hydrogen evolution reaction in natural seawater. *J. Am. Chem. Soc.* **2024**, *146*, 34711-34719.

[7]Sha, Q.; Wang, S.; Yan, L.; Feng, Y.; Zhang, Z.; Li, S.; Guo, X.; Li, T.; Li, H.; Zhuang, Z.; Zhou, D.; Liu, B.; Sun, X. 10,000-h-stable intermittent alkaline seawater electrolysis. *Nature* **2025**, *639*, 360-367.

[8]Wang, T.; Wei, X.; Cheng, Z.; Li, X.; Liu, K.; Ming, L.; Zhang, L.; Lyu, J.; Pan, K.; Li, Z.; Li, R.; Wang, S.; Chen, C.; Kou, Z. In situ constructed chromate cover stabilizes seawater oxidation via competitively repelling chloride ions. *Nano Res.* **2025**, *18*, 94907952.

[9]Yu, L.; Ning, M.; Wang, Y.; Yuan, C.; Ren, Z. Direct seawater electrolysis for hydrogen production. *Nat. Rev. Mater.* **2025**, *10*, 857-873.

[10]Miao, D.; Li, J.; Ren, J.; Chen, Z. Exploring the potential of Ni-based hydrogen evolution catalysts in anion exchange membrane water electrolyzer. *Adv. Mater.* **2026**, *0*, e20491.

[11]Lu, J.; Yu, Z.; Wei, X.; Zhang, X.; Wang, X.; Liu, K.; Cai, Y.; Pan, H.; Liu, D.; Wang, Z. Fe/Co Co-doping engineering for corrosion-resistant and effective seawater electrolysis. *Adv. Mater.* **2026**, *38*, e15156.

[12]Zhang, X.-L.; Yu, P.-C.; Sun, S.-P.; Shi, L.; Yang, P.-P.; Wu, Z.-Z.; Chi, L.-P.; Zheng, Y.-R.; Gao, M.-R. In situ ammonium formation mediates efficient hydrogen production from natural seawater splitting. *Nat. Commun.* **2024**, *15*, 9462.

[13]Yin, Q.; Sun, J.; Fan, J.; Xia, J.; Chen, Y. Study on hydrogen evolution performance of Pt-Co/NF composite electrodes with different mass ratios. *Electrochem. Commun.* **2026**, *182*, 108096.

[14]Vadivel, N.; Govindasamy, M.; Murthy, A. P.; Kuo, C. Next-generation $CoMoS_3$/carbon sphere nanoflower catalyst for sustainable hydrogen production through urea oxidation-assisted water electrolysis. *Electrochem. Commun.* **2026**, *183*, 108102.

[15]Tian, F.; Geng, S.; Li, M.; Qiu, L.; Wu, F.; He, L.; Sheng, J.; Zhou, X.; Chen, Z.; Luo, M.; Liu, H.; Yu, Y.; Yang, W.; Guo, S. Synergetic oxidized Mg and Mo sites on amorphous Ru metallene boost hydrogen evolution electrocatalysis. *Adv. Mater.* **2025**, *37*, 2501230.

[16]Yang, Y.; Pang, D.; Wang, C.; Fu, Z.; Liu, N.; Liu, J.; Wu, H.; Jia, B.; Guo, Z.; Fan, X.; Zheng, J. Vacancy and dopant Co-constructed active microregion in Ru–MoO_{3-x}/Mo_2AlB_2 for enhanced acidic hydrogen evolution. *Angew. Chem. Int. Ed.* **2025**, *64*, e202504084.

[17]Zhao, J.; Urrego-Ortiz, R.; Liao, N.; Calle-Vallejo, F.; Luo, J. Rationally Designed Ru Catalysts Supported on TiN for highly efficient and stable hydrogen evolution in alkaline conditions. *Nat. Commun.* **2024**, *15*, 6391.

[18]Chen, G.; Lu, R.; Zhuang, Z.; Fei, H.; Li, X.; Zhang, X.; Ma, C.; Weng, J.; Wang, J.; Shang, J.; Gan, T.; Wang, Y.; Wang, Z.; Han, Y. Heterophase RuO_2 oxygen evolution catalyst for durable proton exchange membrane water electrolysis. *Sci. Adv.* **2025**, *11*, eaea4543.

[19]Liu, Y.; Wang, L.; Shamraienko, V.; Röder, F.; Wrzesińska-Lashkova, A.; Vaynzof, Y.; Zhang, X.; Eychmüller, A. Tuning the adsorption of H and OH on Ruthenium aerogel to boost the alkaline hydrogen evolution. *Angew. Chem. Int. Ed.* **2025**, *64*, e202513970.

[20]Xu, J.; Kao, C.-C.; Gao, F.; Wang, P.; Shen, H.; Wang, Z.; Zheng, Y.; Qiao, S.-Z. Operando insights into bridging oxygen-driven RuO_x lattice collapse and its mitigation strategy for durable industrial PEMWE. *Angew. Chem. Int. Ed.* **2026**, *65*, e20766.

[21]Liang, J.; Zhao, Y.; Yang, C.; Zhu, S.; Wang, L.; Xu, K.; Mu, X.; Han, Y.; Liu, Z.; Zhao, Z.; Liu, W.; Li, F.; Peng, Z.; Tse, E. C. M.; Liu, Q.; Gao, J.; Li, Q.; Li, J.; Liu, J. Dual-site cobalt-doped RuO_2/TiO_2 electrocatalyst enables stable and cost-efficient acidic oxygen evolution for PEM water electrolysis. *J. Am. Chem. Soc.* **2025**, *147*, 39781-39795.

[22]Liu, T.; Wang, L.; Chen, B.; Liu, H.; Wang, S.; Feng, Y.; Zhang, J.; Yin, Y.; Guiver, M. D. Modulating built-in electric field strength in Ru/RuO_2 interfaces through Ni doping to enhance hydrogen conversion at ampere-level current. *Angew. Chem. Int. Ed.* **2025**, *64*, e202421869.

[23]Guan, S.; Liu, Y.; Liu, S.; Zhuang, Z.; Shen, R.; Zhang, H.; Liang, E.; Fan, Y.; Jiang, J.; Liu, B.; Wang, Y.; Wang, D.; Li, B. MXene-supported Ru-Ni: a common active site for hydrolysis, hydrogen oxidation, and hydrogenation. *Angew. Chem. Int. Ed.* **2025**, *64*, e202506869.

[24]Sukanya, R.; Karthik, R.; Al Mahmud, A.; Dempsey, E.; Ranjith Kumar, D.; Breslin, C. B.; Shim, J.-J. Synergistic interface of Nb-doped $MoSe_2$ and NiTe heterostructure enables efficient electrocatalysis for hydrogen evolution. *Electrochem. Commun.* **2025**, *180*, 108061.

[25]Sukanya, R.; Karthik, R.; Al Mahmud, A.; Kumar, D. R.; Kamaraj, E.; Breslin, C. B.; Shim, J.-J. Vanadium-doped $MoSe_2$ nanosheets: Induced lattice contraction and enhanced conductivity for superior hydrogen evolution reaction. *Electrochem. Commun.* **2025**, *175*, 107916.

[26]Maruta, Y.; Ashitani, H.; Kawaguchi, S.; Ina, T.; Sakata, O.; Kubota, Y.; Yamamoto, T.; Toriyama, T.; Murakami, Y.; Mukoyoshi, M.; Kitagawa, H.; Kusada, K. Revealing dynamic structural changes in platinum-group-metal nanoparticles during the catalytic hydrogen evolution reaction. *J. Am. Chem. Soc.* **2025**, *147*, 36934-36939.

[27]Lu, Z.; Wang, Q.; Wu, S.; Gao, Q.; Wu, H.; Liu, S.; Wu, L.; Ma, X. Visualizing orbital-level d-band modulation in RuCoN nanoalloys anchored on N-doped carbon nanotubes for efficient alkaline AEM water electrolysis. *Nano Res.* **2026**, *19*, 94908263.

[28]Zhang, M.; Luo, X.; Zhou, D.; Wang, S.; Chen, S.; Du, Y.; Zhuang, Z.; Yang, J.; Zhu, W.; Liu, S.; Wang, D.; Dai, Z. Multiscale manipulation of functional imperfection atomic interfaces. *Acc. Chem. Res.* **2026**, *59*, 322-336.

[29]Zheng, X.; Zheng, X.; Gao, M.; Liu, Y.; Pan, H.; Sun, W. Platinum-nickel oxide cluster-cluster heterostructure enabling fast hydrogen evolution for anion exchange membrane water electrolyzers. *Angew. Chem. Int. Ed.* **2025**, *64*, e202422062.

[30]Sun, K.; Mao, W.; Jin, L.; Shi, W.; Niu, W.; Wei, C.; He, Y.; Yan, Q.; Wang, R.; Li, Y.; Zhang, B. Enhancing heterointerface coupling for durable industrial-level proton exchange membrane water electrolysis. *Angew. Chem. Int. Ed.* **2025**, *64*, e202502250.

[31]Yu, M.; Ye, Q.; Xiao, L.; Zeng, X.; Wang, F.; Abdukayum, A.; Zuo, C.; Liu, W.; Li, N.; Hu, G.; Zhao, X. Copper phosphide coupled with amorphous ruthenium on scaffold surfaces synergistically enhances hydrogen production. *Nano Res.* **2026**, https://doi.org/10.26599/NR.2026.94908527.

[32]Xiong, Z.; Kobayashi, K.; Miyawaki, A.; Teranishi, S.; Hibino, T. Electrochemical production of methanol and hydrogen from biomass waste. *Electrochem. Commun.* **2025**, *171*, 107862.

[33]He, Q.; Ge, B.; Zhou, Y.; Mou, L.; Wu, C.; Liu, D.; Jiang, J.; Song, L. Iron-doped ruthenium with a good interfacial environment achieving superior hydrogen evolution activity under alkaline conditions. *Energy Environ. Sci.*, **2025**, *18*, 1984-1991.

[34]Ge, Y.; Sun, L.; Xu, X.; Fu, C.; Yin, Z.; Zhou, Q.; Shi, P.; Yang, W.; Liu, B. Charge-spin-orbit modulated carbon-encapsulated FeP/Fe_3O_4 hetero-junctions for ultrafast and stable conversion of low-concentration nitrate to ammonia. *Angew. Chem. Int. Ed.* **2026**, *65*, e19571.

[35]Wang, H.; Jiao, Y.; Zhang, G.; Ma, W.; Fan, W.; Liu, X.; Zhao, Y.; Xie, H.; Ma, W.; Zong, X. Stabilizing electron-deficient Ru nanoclusters via strong electronic metal-support interaction for practical anion-exchange membrane electrolyzer. *Adv. Funct. Mater.* **2025**, *35*, 241861.

[36]Zhang, W.; Li, C.; Cao, Y.; Ji, J.; Li, Z.; Niu, Z.; Gu, H.; Braunstein, P.; Lang, J. Electronic engineering of Co-Ru diatomic sites and Ru nanoparticles for synergistic promotion of hydrogen evolution. *Nano Res.* **2024**, *17*, 3714-3723.

[37]Lu, Q.; Zou, X.; Wang, J.; Wang, Y.; Shao, Z. Ruthenium-based composites: unlocking the application potential of rechargeable zinc-air batteries. *Energy Storage Mater.* **2026**, *84*, 104880.

[38]Liu, J.; Yang, J.; Dou, Y.; Liu, X.; Chen, S.; Wang, D. Deactivation

mechanism and mitigation strategies of single-atom site electrocatalysts. *Adv. Mater*. **2025**, *37*, 2420383.

[39]Gong, C.; Li, W.; Du, X.; He, X.; Wang, D.; Chen, H.; Fang, W.; Zhao, L.; Chai, Y. Manipulating spin polarization by in-situ reconstructed amorphous/crystalline CoFe-LDH for efficient electrocatalytic water splitting. *Nano Res*. **2025**, *9*, 94907668.

[40]Xia, J.; Xu, J.; Yu, B.; Liang, X.; Qiu, Z.; Li, H.; Feng, H.; Li, Y.; Cai, Y.; Wei, H.; Li, H.; Xiang, H.; Zhuang, Z.; Wang, D. A metal-sulfur-carbon catalyst mimicking the two-component architecture of nitrogenase. *Angew. Chem. Int. Ed*. **2024**, *63*, e202412740.

[41]Zhu, K.; Yang, H.; Guo, G.; Wang, Y.; Tan, W.; Ma, F.; Zhang, H.; Peng, S. Pd single atoms/clusters at the oxygen defect-rich WO_xC nanowire structure facilitate H adsorption and desorption for efficient and stable hydrogen evolution reaction. *ACS Catal*. **2025**, *15*, 9563-9573.

[42]Vivier, V.; Oraze, M.-E. Impedance analysis of electrochemical systems. *Chem. Rev*. **2022**, *122*, 11131-11168.

[43]Zhang, J.; Cai, X.; Li, X.; Zhang, C.; Ke, S.; Zhang, C.; Wu, Y.; Lin, R. Low loading of IrO_2/TiO_2 enabled by Pd promoter in acidic water electrolysis. *Nano Res*. **2025**, *18*, 94908065.

[44]Wang, H.; Cao, W.; Sun, H.; Du, X.; Wang, Y.; Li, J.; Wu, L.; Liu, G.; Song, S. Dual regulation via oxyphilic dysprosium doping: stabilizing oxide support and customizing catalytic pathway for ampere-level alkaline hydrogen evolution. *Angew. Chem. Int*. Ed. **2026**, e19688.

[45]Chang, B.; Liu, X.; Zuo, S.; Ren, Y.; He, J.; Wang, D.; Lei, Y.; Hu, M.; Li, W.; Khan, M.-A; Aleisa, R.; Hu, R.; Hou, Y.; Liu, H.; Zhou, W.; Lai, Z.; Alshareef, H.-N.; Zhang, H. Dynamic construction of a durable epitaxial catalytic layer for industrial alkaline water splitting. *Nat. Commun*. **2025**, *16*, 7959.

[46]Xie, L.; Wang, L.; Liu, X.; Chen, J.; Wen, X.; Zhao, W.; Liu, S.; Zhao, Q. Flexible tungsten disulfide superstructure engineering for efficient alkaline hydrogen evolution in anion exchange membrane water electrolysers. *Nat. Commun*. **2024**, *15*, 5702.

[47]Zhou, S.; Cao, W.; Shang, L.; Zhao, Y.; Xiong, X.; Sun, J.; Zhang, T.; Yuan, J. Facilitating alkaline hydrogen evolution kinetics via interfacial modulation of hydrogen-bond networks by porous amine cages. *Nat. Commun*. **2025**, *16*, 1849.

[48]Yang, C.; Gao, Y.; Xing, Z.; Shu, X.; Zhuang, Z.; Wang, Y.; Zheng, Y.; Li, S.; Cheng, C.; Wang, D.; Zhang, J. Bioinspired Sulfo oxygen bridges optimize interfacial water structure for enhanced hydrogen oxidation and evolution reactions. *Nat. Commun*. **2025**, *16*, 6459.

[49]Zhou, Y.; Ibáñez-Alé, E.; López, N.; Cuenya, B.-R.; Kley, C.-S. Carbonate anions and radicals induce interfacial water ordering in CO_2 electroreduction on gold. *Nat. Chem*. **2025**, https://doi.org/10.1038/s41557-025-01977-8.

Electronic Supplementary Material

Construction of $Fe^{\delta+}$–$Ru^{\delta-}$ synergistic interface enabling efficient and stable hydrogen evolution in versatile electrolytes

Min Yu, Ziqin Xu, Yuyue Wang, Hao Chen, Kuaibing Wang, Hongjing Zhu, Yi Song, Changyun Chen ✉, and Guangxiang Liu ✉

Jiangsu Key Laboratory of Zero-Carbon Energy Development and System Integration, Nanjing Xiaozhuang University, Nanjing 211171, China

✉ Address correspondence to Changyun Chen, cychen@njxzc.edu.cn; Guangxiang Liu, liugx@njxzc.edu.cn

Supporting information to https://doi.org/10.26599/NR.2026.94908737

1 Characterization instruments

Materials were characterized using the following techniques and instruments. X-ray diffraction (XRD) patterns were recorded on a Bruker D8 Advance diffractometer with Cu Kα radiation (λ = 1.5406 Å) in the 2θ range of 5–90°. Raman spectra were acquired on a Renishaw inVia spectrometer using a 532 nm laser. Nitrogen adsorption-desorption isotherms were measured at 77 K using a Micromeritics ASAP 2460 analyzer; samples were degassed at 150 °C for 6 h prior to measurement. The specific surface area was calculated using the Brunauer–Emmett–Teller (BET) method, and pore size distribution was derived from the adsorption branch using the Barrett–Joyner–Halenda (BJH) model. Transmission electron microscopy (TEM), high-resolution TEM (HRTEM), and energy-dispersive X-ray spectroscopy (EDS) mapping were performed on a JEOL JEM-F200 microscope operating at 200 kV. X-ray photoelectron spectroscopy (XPS) was conducted on a Thermo Scientific K-Alpha+ spectrometer with Al Kα radiation (1486.6 eV); all spectra were calibrated using the C 1s peak at 284.8 eV and analyzed using Avantage software.

2 Electrochemical Tests

Electrochemical measurements were carried out using a standard three-electrode configuration on a CHI 760E electrochemical workstation at room temperature (25 ± 1 °C). The working electrode was prepared by drop-casting a homogeneous catalyst ink (5 mg catalyst in 950 μL ethanol and 50 μL 5 wt% Nafion) onto a polished glassy carbon electrode (5 mm diameter). A graphite rod and a saturated calomel electrode (SCE) were used as the counter and reference electrodes, respectively. All potentials reported are referenced to the reversible hydrogen electrode (RHE) after calibration. Before testing, the electrolyte was purged with high-purity N_2 for at least 30 minutes and maintained under a N_2 atmosphere. Linear sweep voltammetry (LSV) was performed at a scan rate of 5 mV s^{-1} with iR compensation. Electrochemical impedance spectroscopy (EIS) was measured from 100 kHz to 0.1 Hz with a 5 mV amplitude at a fixed overpotential. Cyclic voltammetry (CV) at various scan rates (20-200 mV s^{-1}) in the non-faradaic region was used to estimate the electrochemical active surface area (ECSA) via double-layer capacitance (Cdl). Long-term stability was assessed by chronopotentiometry (CP) at a constant current density and by continuous CV cycling.

The turnover frequency (TOF) was calculated according to the following equation (assuming that every metal atom is involved in the catalysis) [1]:

$$TOF=j\times S/(2\times F\times n)$$

where j (mA cm^{-2}) is the measured current density at η =50 mV, S is the surface area of the electrode, the number 2 means 2 electrons mol^{-1} of H_2 evolution, F is the Faraday constant (96485.3 C mol^{-1}), and n is the mole of metal atoms coated on the electrode.

MA (Mass Activity)[2]:

$$MA=j/m$$

where j (mA cm^{-2}) is the measured current density at η =50 mV, m (mg cm^{-2}) = (0.004 mL×5 mg mL^{-1})/(π×0.15^2), a rotating disc electrode with a radius of 1.5 mm, the concentration of the prepared sample was 5 mg mL^{-1}, 4 μL (0.004 mL) is the amount to add to a prepared sample.

In-situ Raman spectroscopy was conducted using a confocal Raman spectrometer equipped with a 532 nm laser light source,

combined with a custom in-situ electrochemical cell, allowing for the synchronous collection of both spectral signals and electrochemical responses during the electrochemical process. The catalyst ink was evenly drop-coated onto the surface of the glassy carbon working electrode, forming a three-electrode system with a platinum wire counter electrode and a Hg/HgO reference electrode. The electrolytes used were 1.0 M KOH solution, alkaline seawater, and alkaline wastewater. Electrochemical testing was performed with a CHI 760E workstation, with high-purity nitrogen gas continuously bubbled into the electrolyte for 30 minutes prior to testing to thoroughly remove dissolved oxygen. During the test, the working electrode potential was controlled by a potentiostatic program, and once the system current stabilized, Raman spectral data was synchronously collected.

3 DFT details

All density functional theory (DFT) calculations were performed using the Vienna Ab initio Simulation Package (VASP) with the projector augmented wave (PAW) method. The generalized gradient approximation (GGA) in the form of the Perdew–Burke–Ernzerhof (PBE) functional was employed to describe the exchange–correlation interaction. Van der Waals corrections were included using the DFT-D3 method of Grimme to account for non-local dispersion interactions. A plane-wave cutoff energy of 450 eV was used throughout all calculations. The Brillouin zone was sampled using a Γ-centered k-point mesh with a density of $2\pi \times 0.03$ Å^{-1} for structural relaxations and $2\pi \times 0.02$ Å^{-1} for electronic property calculations. The convergence criteria for electronic self-consistency and ionic relaxation were set to 1×10^{-5} eV and 0.02 eV Å^{-1}, respectively.

To simulate the FeRu-ERBC catalyst, three representative structural models were constructed: (1) Ru/ideal C, representing Ru clusters supported on an ideal graphene sheet; (2) FeRu/ideal C, representing Fe_3O_4 and Ru clusters on an ideal graphene support; and (3) FeRu/defective C, representing Fe single atom and Ru clusters on a defective carbon support containing oxygen, which mimics the actual ERBC surface. All models were built using a 4 × 4 graphene supercell with a vacuum layer of 15 Å along the z-direction to avoid periodic interactions. The FeRu clusters were constructed based on the experimentally determined Fe/Ru atomic ratio and the observed substitutional structure.

Address correspondence to Changyun Chen,; Guangxiang Liu,

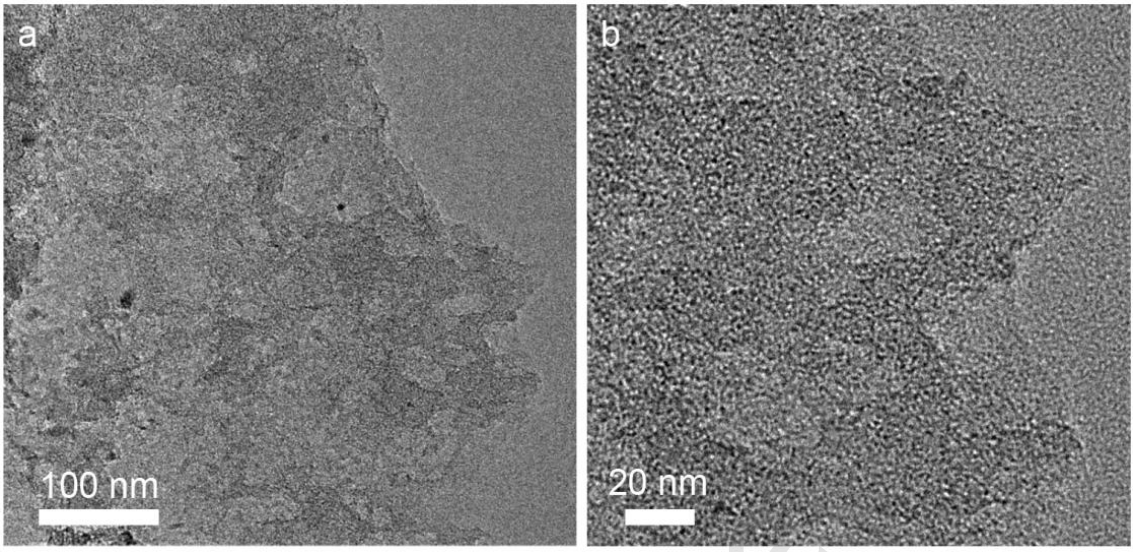

Figure S1 (a, b) TEM images of Fe-ERBC.

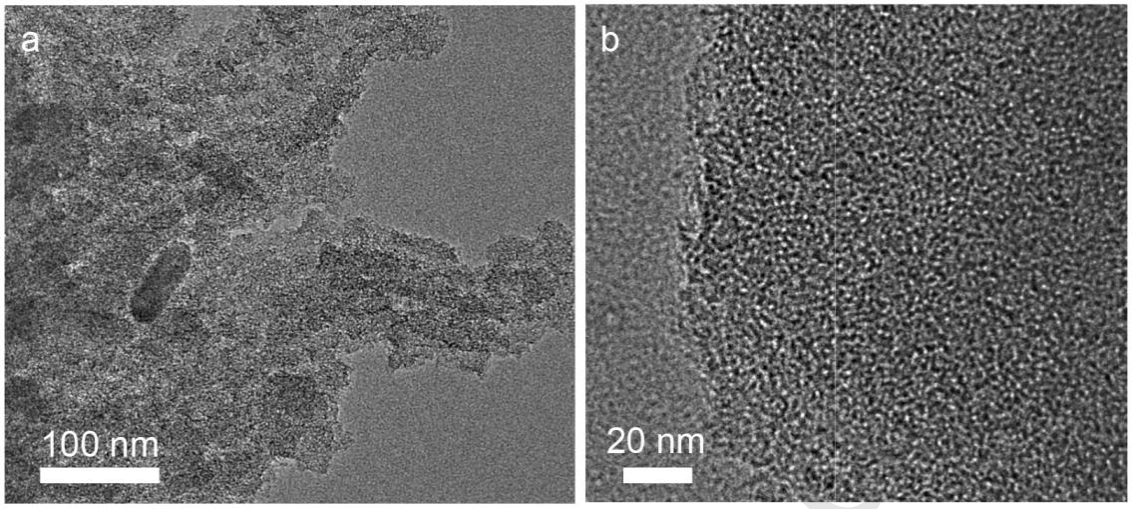

Figure S2 (a, b) TEM images of Fe-AC.

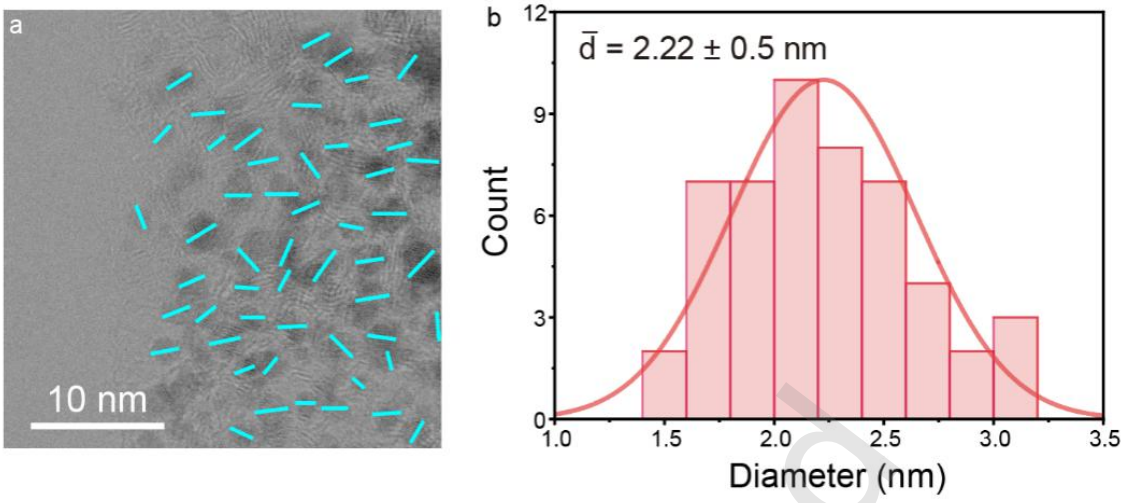

Figure S3 (a) TEM images of FeRu-ERBC. (b) Particle size distribution (measurements of more than 60 particles).

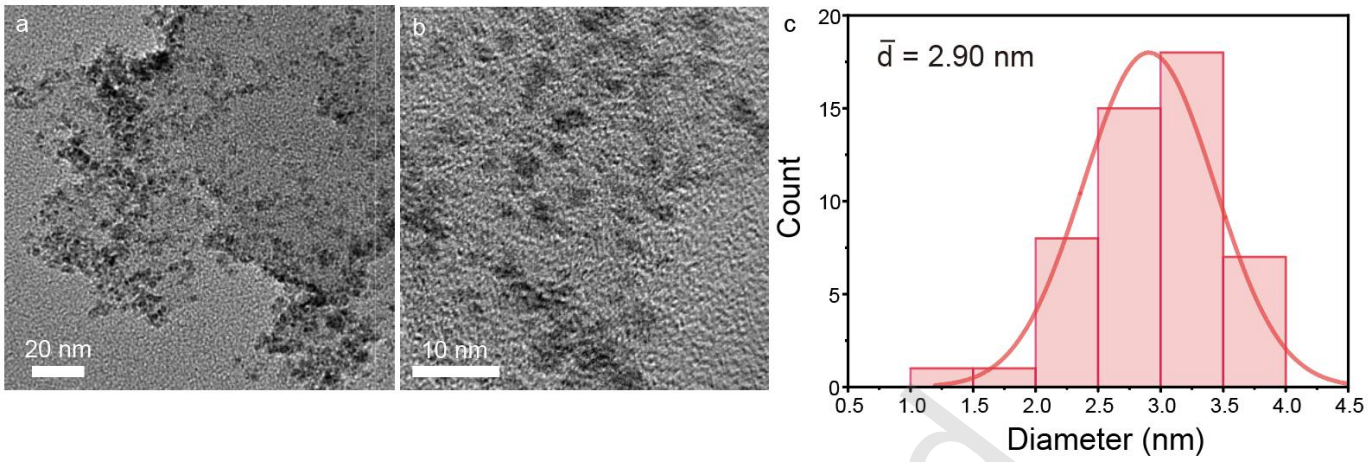

Figure S4 (a, b) TEM images of FeRu-AC. (c) Particle size distribution.

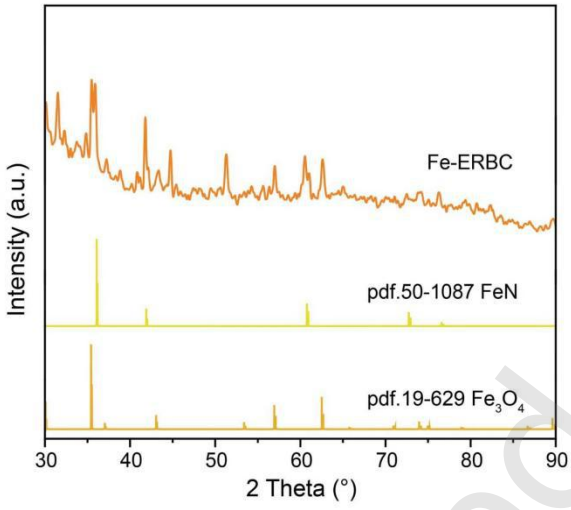

Figure S5 XRD patterns of Fe-ERBC.

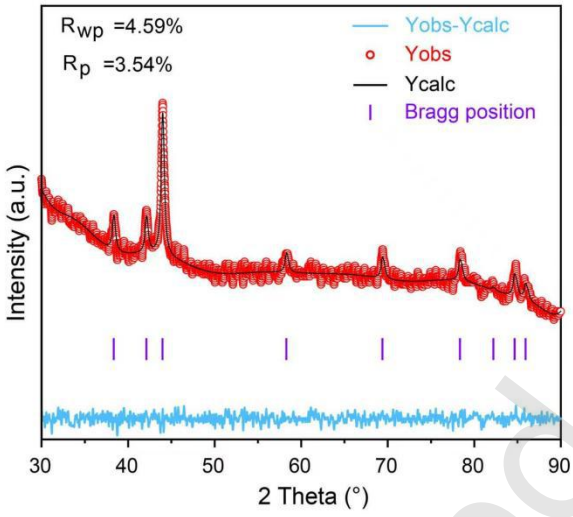

Figure S6 Rietveld refinement pattern of FeRu-ERBC.

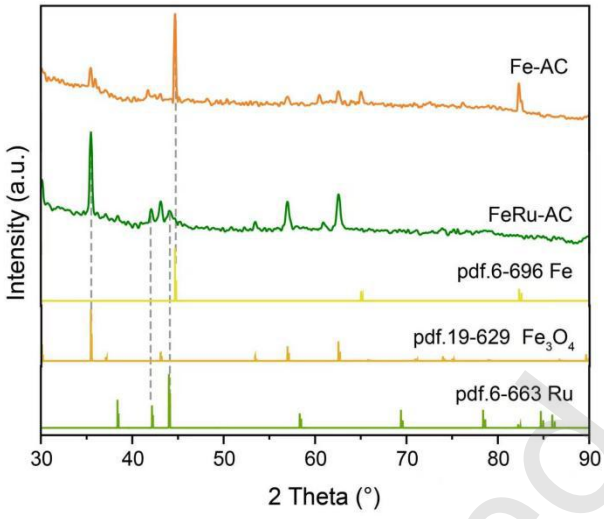

Figure S7 XRD patterns of Fe-AC, FeRu-AC.

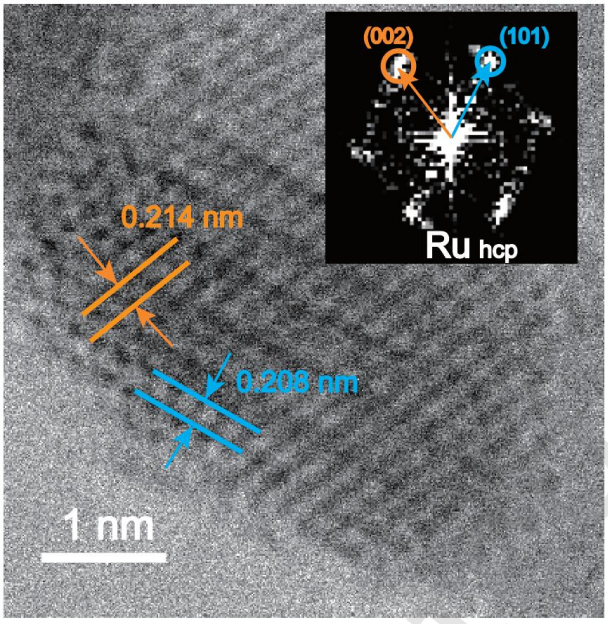

Figure S8 HRTEM images of FeRu-ERBC. The illustration is an FFT image, with lattice fringes marked.

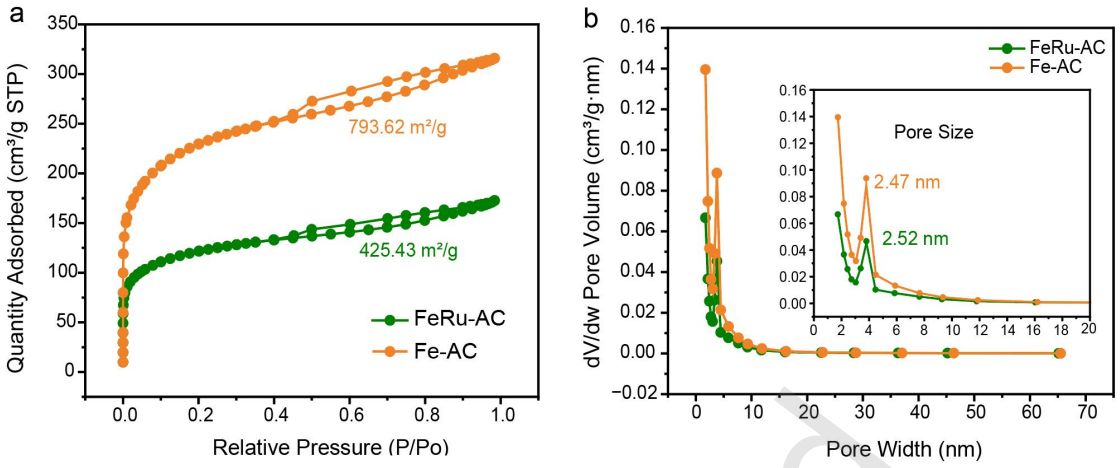

Figure S9 (a) N_2 adsorption isotherms for FeRu-AC and Fe-AC. (b) Corresponding pore size distribution.

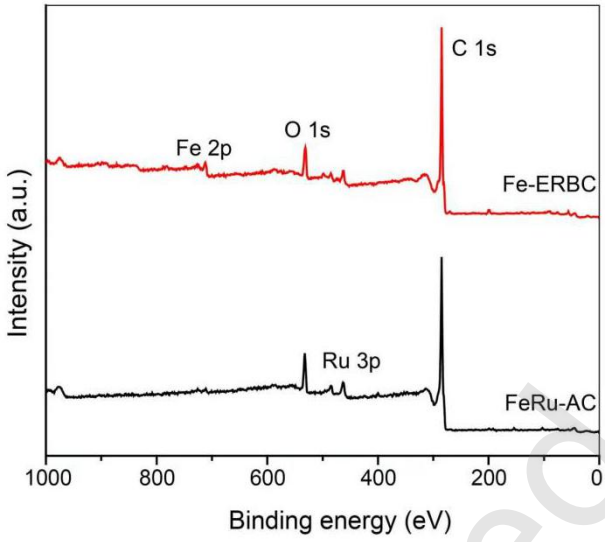

Figure S10 XPS spectra of FeRu-AC and FeRu-ERBC.

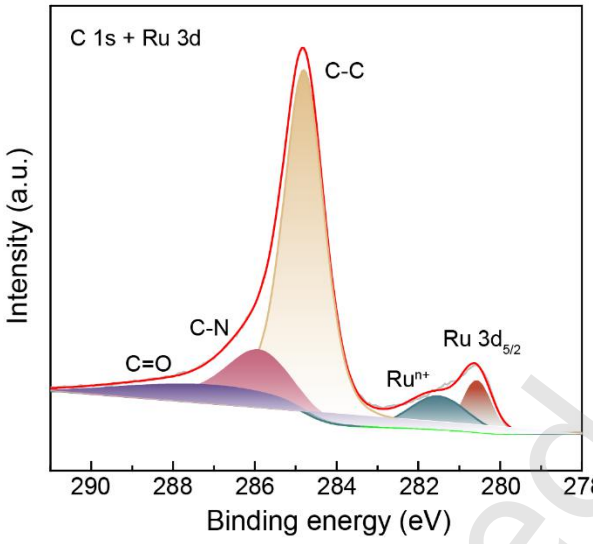

Figure S11 High-resolution Ru 3d XPS spectrum of FeRu-ERBC.

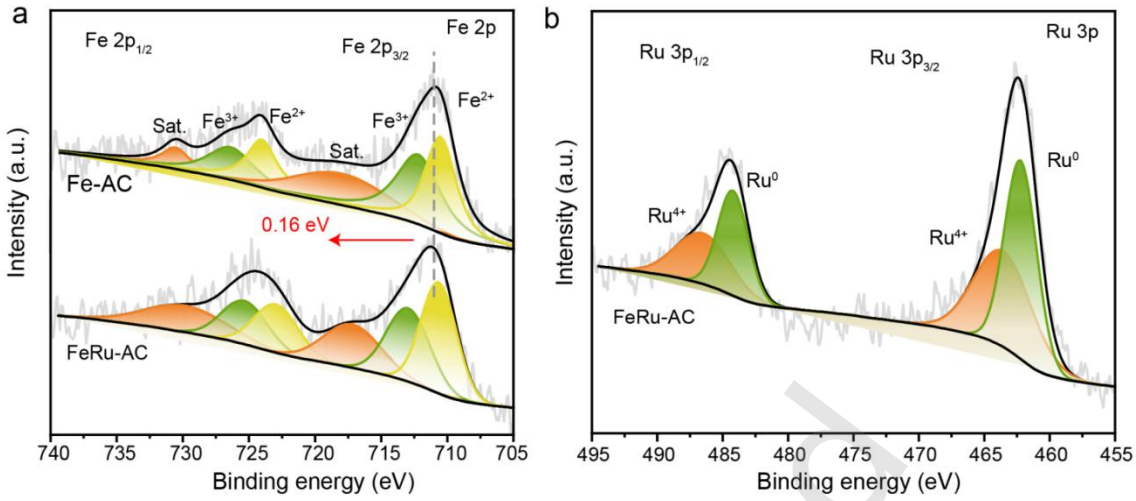

Figure S12 (a) Fe 2p XPS spectrum of FeRu-AC, Fe-AC. (b) Ru 3p XPS spectrum of FeRu-AC.

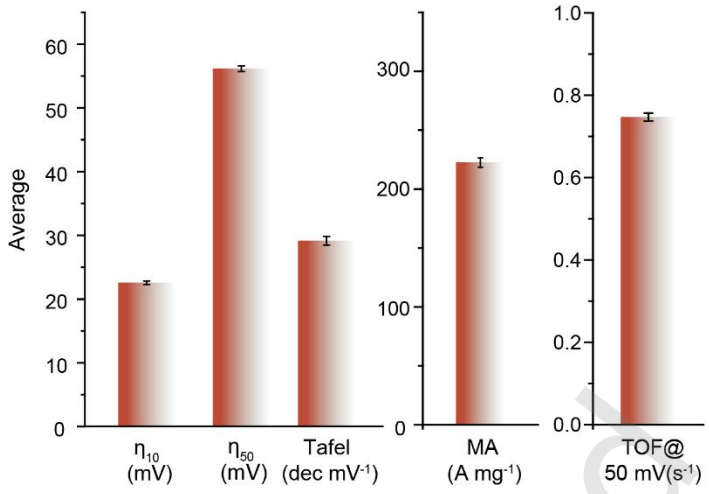

Figure S13 Comparison of key HER performance parameters of FeRu-ERBC with error bars derived from three independent measurements.

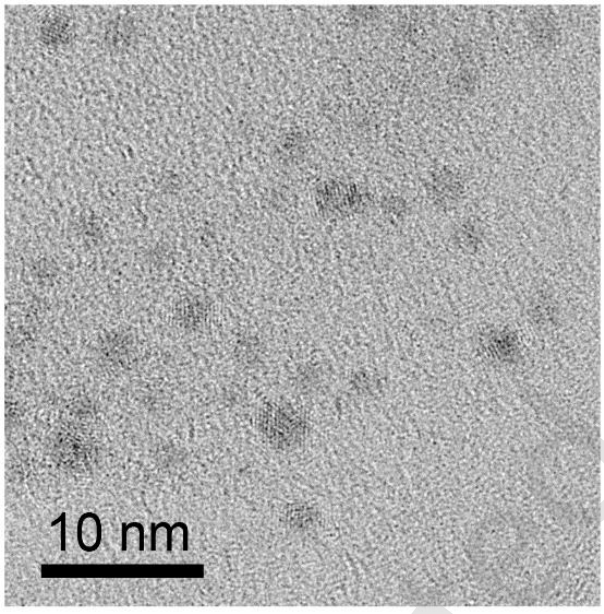

Figure S14 TEM image of FeRu-ERBC after 120-hour stability test.

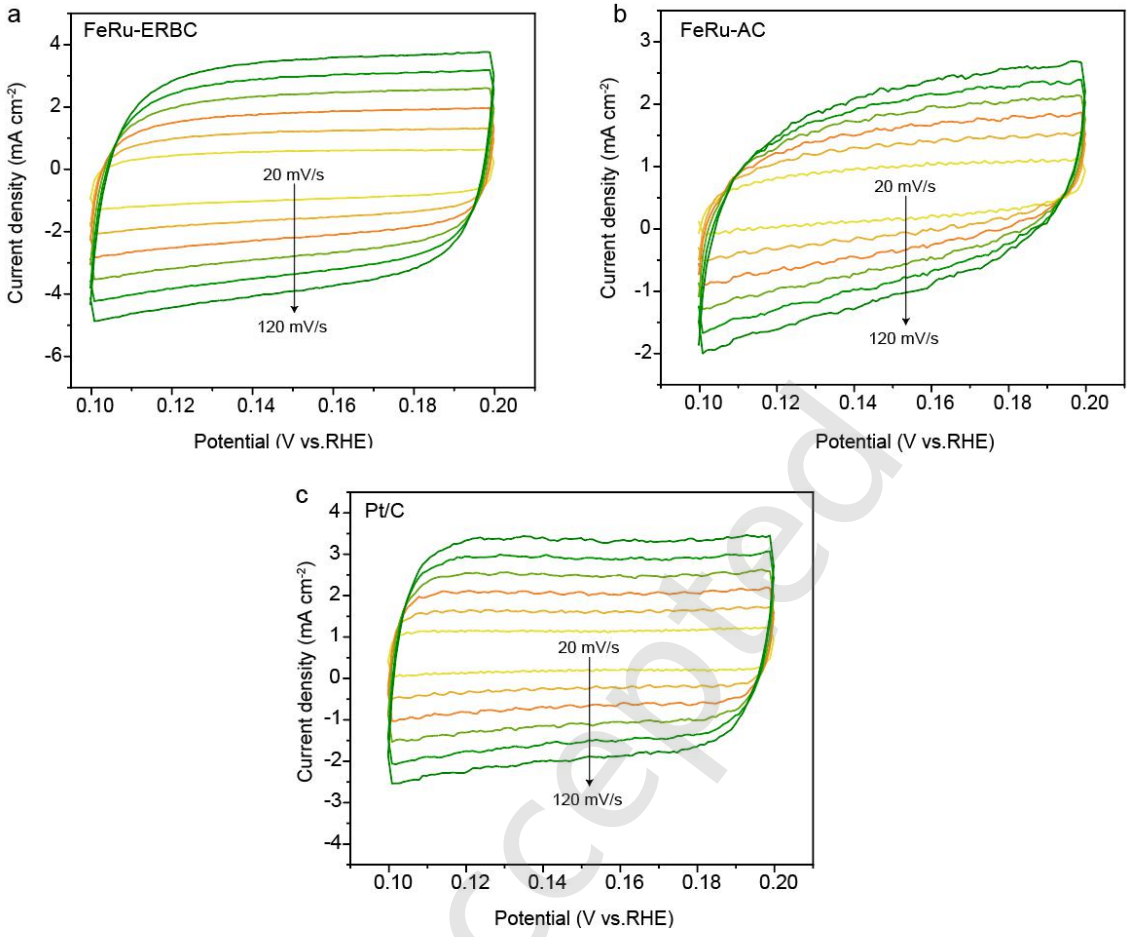

Figure S15 Cyclic voltammograms (CV) curves of (a) FeRu-ERBC, (b) FeRu-AC, (c) Pt/C at different scan rates.

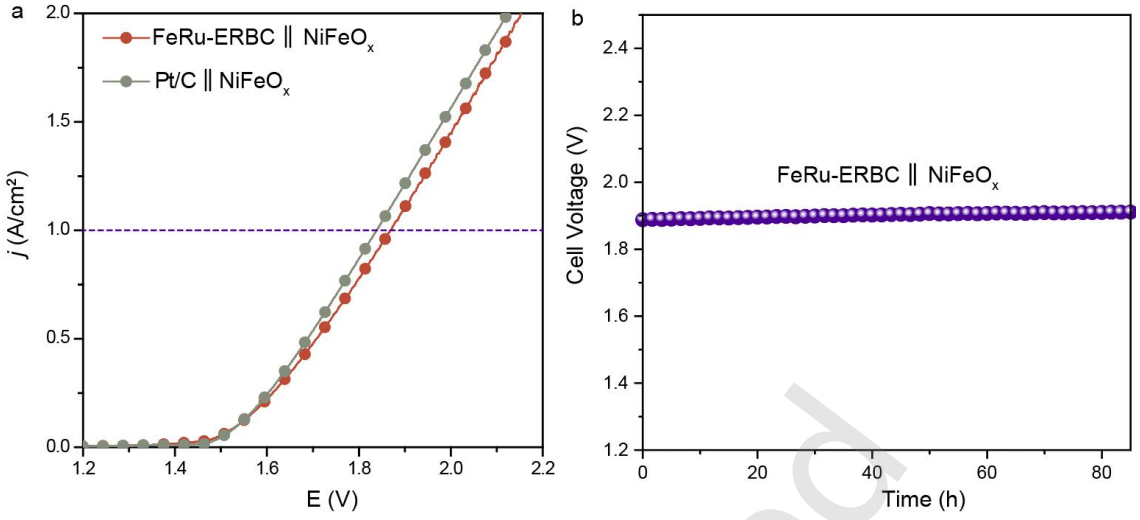

Figure S16 (a) Polarization curves and (b) stability test of FeRu-ERBC and Pt/C as cathode catalysts in an alkaline electrolyzer.

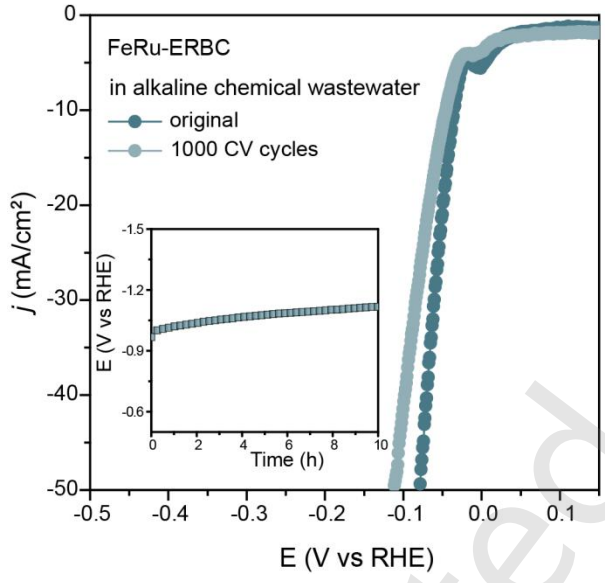

Figure S17 Cyclic voltammetry cycling stability test of FeRu- ERBC in alkaline chemical wastewater; the inset shows the corresponding chronopotentiometry test curve.

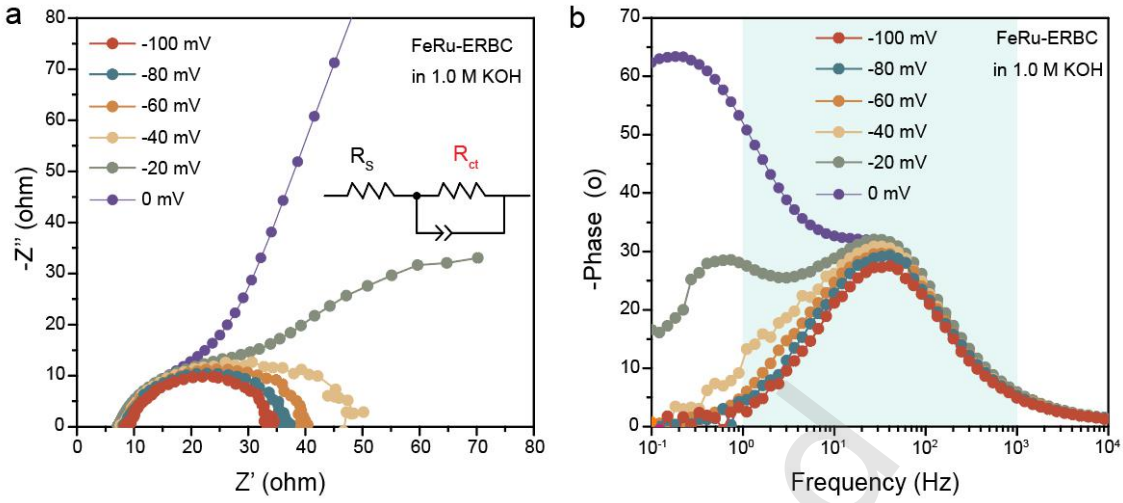

Figure S18 (a) Nyquist plots of FeRu-ERBC measured at different applied potentials in 1.0 M KOH. (b) Corresponding Bode plots.

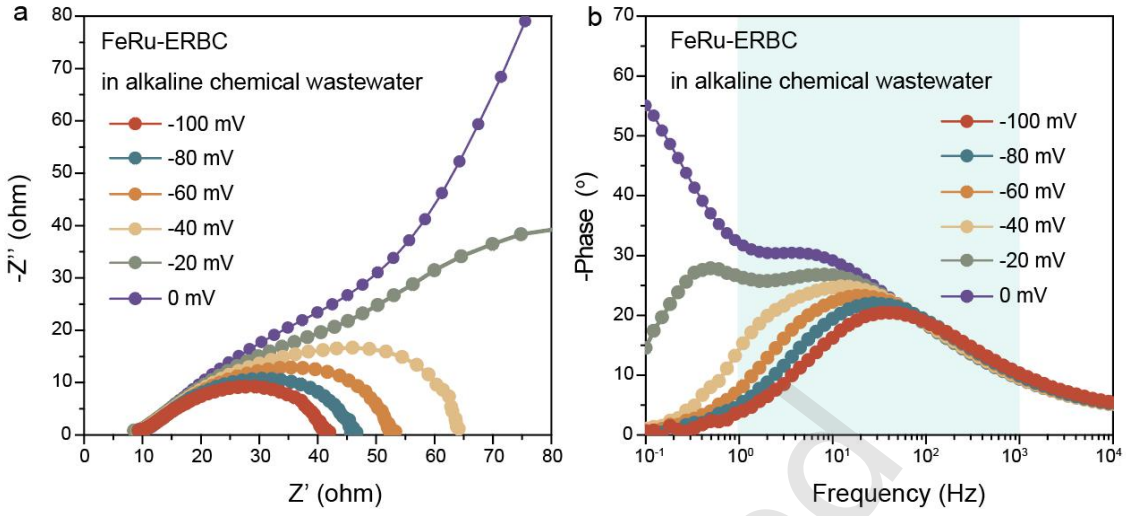

Figure S19 (a) Nyquist plots of FeRu-ERBC measured at different applied potentials in alkaline seawater. (b) Corresponding Bode plots.

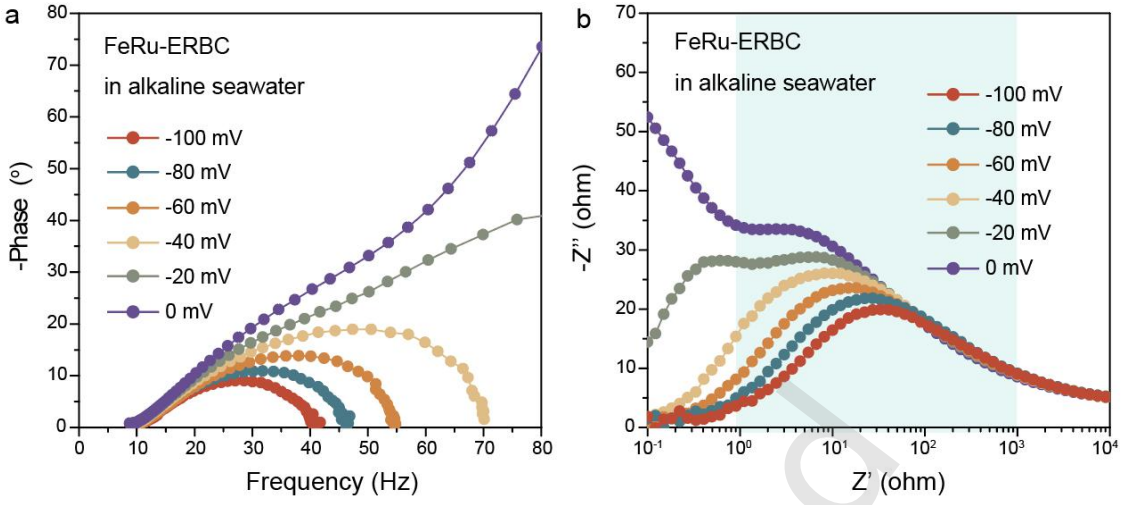

Figure S20 (a) Nyquist plots of FeRu-ERBC measured at different applied potentials in alkaline chemical wastewater. (b) Corresponding Bode plots.

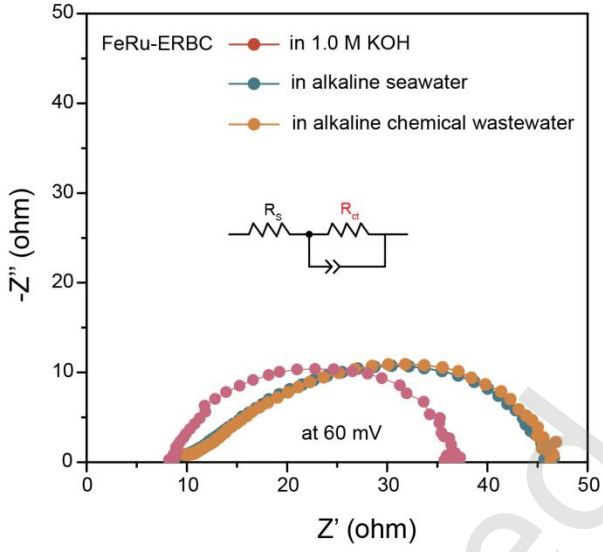

Figure S21 Comparison of Nyquist plots for FeRu-ERBC at 40 mV measured in different electrolytes.

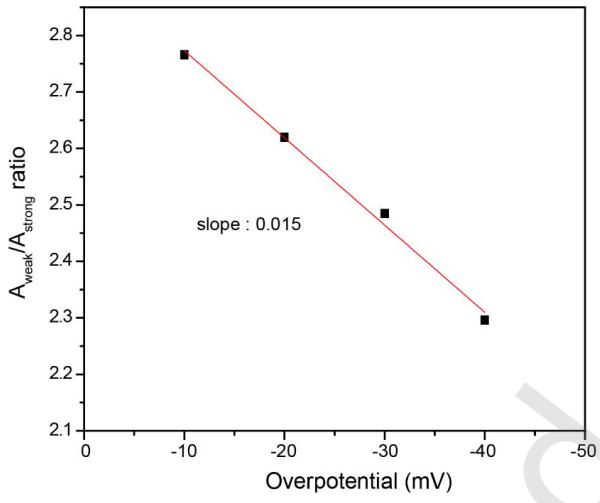

Figure S22 Linear correlation between the fitted peak area of hydrogen-bonded water and the applied potential.

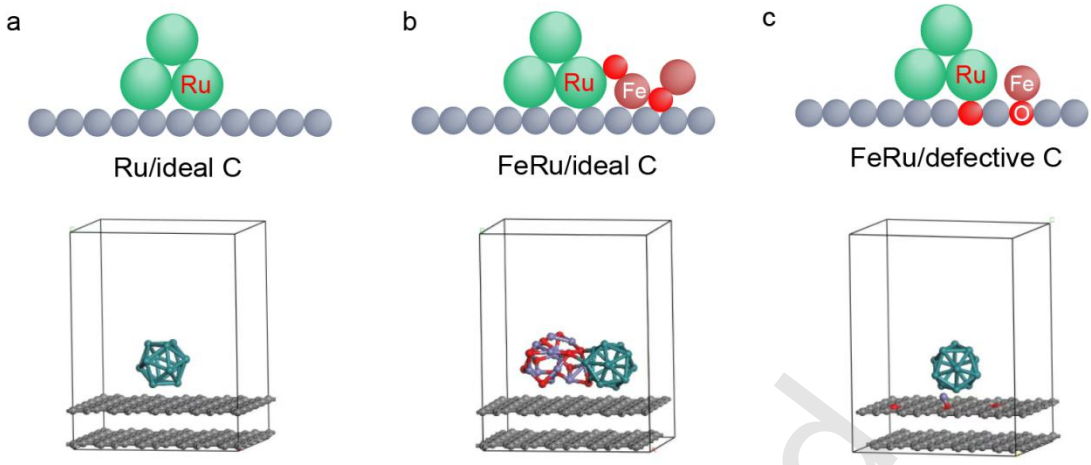

Figure S23 Structural schematic diagrams of the (a) Ru/ideal C, (b) FeRu/ideal C, and (c) FeRu/defective C models.

Table S1 ICP-OES analysis results of Fe-ERBC, FeRu-ERBC, Fe-AC and FeRu-AC.

Samples	Elements	wt%
Fe-ERBC	Fe	48.80
FeRu-ERBC	Fe	2.27
	Ru	10.03
Fe-AC	Fe	40.60
FeRu-AC	Fe	24.80
	Ru	13.24

Table S2 Comparison performances of FeRu-ERBC and FeRu-AC for HER in 1.0 M KOH.

	FeRu-ERBC	FeRu-AC
η 10 (mV)	22.7	65.93
η50 (mV)	56.4	154.5
Tafel (mV dec^{-1})	29.0	68.7
MA (A mg^{-1})	224.2	3.4
TOF (s^{-1})	0.75	0.01

Table S3 Performance comparison of FeRu-ERBC with the other reported HER catalysts.

Catalysts	Overpotential (mV)	MA	TOF	Stability	Ref.
FeRu-ERBC	22.7	224.17 A mg^{-1} at 50 mV	0.75 s-1 at 50 mV	120 h	This work
$Ni_3N@W_5N_4$	60			100 h	*Angew. Chem. Int. Ed.* **2025**, *64*, e202414647
$FeP@NiCoP/Mo_4P_3$	72			100 h	*Adv. Funct. Mater.* **2025**, *35*, 2507225
MoO_2/Ni_3S_2/NF	74			24 h	*Nano Energy* **2024**, *122*, 109299
I-Ni@C	78			80 h	*J. Am. Chem. Soc.* **2024**, *146*, 26844
Mn-doped Ni_2P/Fe_2P	90			200 h	*Chem. Eng. J.* **2023**, *454*, 140061
Pt-NiCo LDO	92				*Adv. Funct. Mater.* **2024**, *34*, 2405919
$V_{0.3}$-NiS/NiS_2	94		0.528 s^{-1} at 1.6 V	100 h	*Adv. Energy Mater.* **2023**, *13*, 2300978
Ni/MoN/CC	95				*J. Colloid Interface Sci.* **2025**, *686*, 68
MoP-QDs@PC	98.8		0.91 s^{-1} at 200 mV	50 h	*Chem. Eng. J.* **2023**, 454, 140105
$MCu_{0.10}$-BNiMo	156			10 h	*Adv. Mater.* **2024**, *36*, 2313156
$PDTA_2@CoLaME$	162			20 h	*Adv. Funct. Mater.* **2024**, *34*, 2313233
Eu_2O_3-NiCo	60		1.56 s^{-1} at 150 mV	24 h	*Adv. Funct. Mater.* **2024**, *34*, 2409324
3DOM-RuSA/NC	36	73.3 mA mg^{-1} at 50 mV	15.97 s^{-1} at 100 mV	500 h	*Small* **2026**, *22*, e10619
Ru/S-Co_3O_4	25		1.87 s^{-1} at 100 mV	＞100 h	*Appl. Catal. B Environ.* **2026**, *382*, 126023
Co_{50}Ni-C/NF	30		0.2 s^{-1} at 10 mV	72 h	*J. Colloid Interface Sci.* **2026**, *707*, 139746
Ru/MoB-BV	40	1.59 A mg^{-1} at 100 mV	0.84 s^{-1} at 100 mV	12 h	*Adv. Mater.* **2026**, *38*, e23202
Pt/Ni $(OH)_2$	26	11.85 A mg^{-1} at 70 mV	13.63 s^{-1} at 70 mV	200 h	*Angew. Chem. Int. Ed.* **2025**, *64*, e202509268

References

[1] Wang, K.; Zhou, J.; Sun, M.; Lin, F.; Huang, B.; Lv, F.; Zeng, L.; Zhang, Q.; Gu, L.; Luo, M.; Guo, S. Cu-Doped heterointerfaced Ru/$RuSe_2$ nanosheets with optimized H and H_2O adsorption boost hydrogen evolution catalysis. *Adv. Mater.* **2023**, *35*, 2300980.
[2] Liang, X.; Zhang, Z.; Wang, Z.; Hu, M.; Cheng, D.; Jiang, Y.; Ren, H.; Shen, F.; Yang, S.; Yang, X.; Jiang, W.; Shi, X.; Ma, Z.; Zhou, K. Breaking the H_2O dissociation-OH desorption scaling relationship in alkaline hydrogen evolution by oxophilic single atom M_1–Ru_n electrocatalysts. *Energy Environ. Sci.* **2025**, *18*, 4302-4311.